GEOTHERMAL FLUID EQUILIBRIUM MODELING: COMPARISON OF WELLHEAD FLUID SAMPLES TO DEEP SAMPLES IN THE REYKJANES SYSTEM, ICELAND

by

RYAN J. SEWARD

A THESIS

Presented to the Department of Geological Sciences
and the Graduate School of the University of Oregon
in partial fulfillment of the requirements
for the degree of
Master of Science

March 2014

THESIS APPROVAL PAGE

Student: Ryan J. Seward

Title: Geothermal Fluid Equilibrium Modeling: Comparison of Wellhead Fluid Samples to Deep Samples in the Reykjanes System, Iceland

This thesis has been accepted and approved in partial fulfillment of the requirements for the Master of Science degree in the Department of Geological Sciences by:

Mark Reed	Chair
Paul Wallace	Member
Alan Remple	Member

and

Kimberly Andrews Espy	Vice President for Research and Innovation; Dean of the Graduate School

Original approval signatures are on file with the University of Oregon Graduate School.

Degree awarded March 2014

THESIS ABSTRACT

Ryan J. Seward

Master of Science

Department of Geological Sciences

March 2014

Title: Geothermal Fluid Equilibrium Modeling: Comparison of Wellhead Fluid Samples to Deep Samples in the Reykjanes System, Iceland

Single phase geothermal fluids sampled in 2007 from 1500m depth in Well RN-12 of the Reykjanes geothermal system in Iceland show large differences in dissolved copper, zinc and iron concentrations when compared with fluid sampled from the wellhead. Equilibrium modeling of the samples taken at depth indicate that the fluid was supersaturated in sulfide minerals even at moderately acidic pH values, suggesting that the deep samples, as collected, are out of equilibrium.

Wellhead sample reconstructions indicate a well-bottom pH of about 5.5 at 295°C, but a pH of 3.6 at saturation with chalcopyrite, bornite, pyrite and sphalerite would be required to account for the large concentrations of Cu, Zn and Fe in the down-well samples. This acidic value needed for the high metal concentrations is not realistic in this naturally buffered system, likely indicating contamination in the downhole analysis.

CURRICULUM VITAE

NAME OF AUTHOR: Ryan J. Seward

GRADUATE AND UNDERGRADUATE SCHOOLS ATTENDED:

University of Oregon, Eugene
Lane Community College, Eugene, Oregon
Chemeketa Community College, Salem, Oregon

DEGREES AWARDED:

Master of Science, 2014, Geology, University of Oregon
Bachelor of Science, 2010, Geology, University of Oregon

AREAS OF SPECIAL INTEREST:

Geothermal geochemistry
Ore Deposits

PROFESSIONAL EXPERIENCE:

Graduate Teaching Fellow, Department of Geological Sciences, University of Oregon, Eugene, 2010-2014

TABLE OF CONTENTS

LIST OF FIGURES

LIST OF TALBES

CHAPTER I
INTRODUCTION

With an increasing global demand for energy resources and counteracting demands to decrease dependence on fossil fuels, the need for alternative energy such as geothermal power should not only remain high but increase with time. Yet the utilization of a natural geothermal system for power production brings challenges at every step. One of these challenges is addressed here; geothermal waters are not pure and easily predictable, but rather are solutions with dissolved solutes that define the complex chemical interactions they undergo. The chemical composition of the fluid influences all aspects of geothermal energy production including: the permeability of the rocks they flow through, the amount of heat carried with the fluid, the longevity of a wellbore and its connecting surface pipe network, and the types of materials used for power production. However, the current understanding of deep fluid from which power producing fluids are derived and the interpretation of their evolution within a system is highly reliant on speculation.

Historically, understanding the chemical state of a geothermal fluid has relied solely on the samples collected where fluid appears at the surface from natural springs or the top of a well. However if one wants to understand the chemical evolution of a geothermal fluid, its starting chemical properties at depth within the reservoir must be extrapolated from these wellhead samples. This is only possible if the fluids were in equilibrium with the rocks at depth and reached the surface with

a tractable change from its reservoir equilibrium state, thus the samples must still hold a chemical signature of their past (Spycher et al., 2014; Wanner et al., 2013).

In recent years the temperature at which geothermal fluids can be sampled from depth has increased to allow direct sampling of single phase geothermal fluid within the well bore below the depth where boiling separates it into the steam and liquid phases seen at the wellhead (Hardardóttir et al., 2009; Rae, Cooke, & Brown, 2011; Simmons & Brown, 2006). In 2007, analyses of downhole samples from three wells in the Reykjanes geothermal system of Iceland revealed dissolved metal concentrations orders of magnitude larger than wellhead samples of the same wells (Hardardóttir et al., 2009). The large difference between these concentrations was attributed to precipitation of sulfide minerals within the well between the downhole sampling depth and wellhead sampling (Hardardóttir, Hannington, Hedenquist, Kjarsgaard, & Hoal, 2010). This study is a detailed look into the relationship between the same wells downhole and wellhead samples using equilibrium modeling and suggests that mineral precipitation between sampling locations is unable to account for the large discrepancy in dissolved metal concentrations.

CHAPTER II
BACKGROUND

1. Location

The Reykjanes geothermal field in the south west of Iceland, Figure 1, is the topic of many recent and current studies in response to its designation as the proposed drilling site for a deep well in search of supercritical fluids(Fridleifsson & Elders, 2005; Friðleifsson & Richter, 2010; Friðleifsson, Sigurdsson, et al., 2013; Marks, Schiffman, Zierenberg, Elders, et al., 2010). The Iceland Deep Drilling Project, IDDP, is a scientific partnership between groups from the Icelandic geothermal industry and Icelandic government, along with an international team of scientists. The IDDP is focused on the goal of exploring unconventional geothermal resources by drilling to the depth needed, approximately 4-5km, to tap a supercritical fluid resource capable of producing an order of magnitude more power than what is possible with traditional 300°C fluids from the same volumetric flow (Friðleifsson, Elders, & Albertsson, 2013). The variety of studies covering Reykjanes provide an excellent framework in which to undertake investigations into the evolving chemical state of geothermal fluids upon ascent from depth to the wellhead.

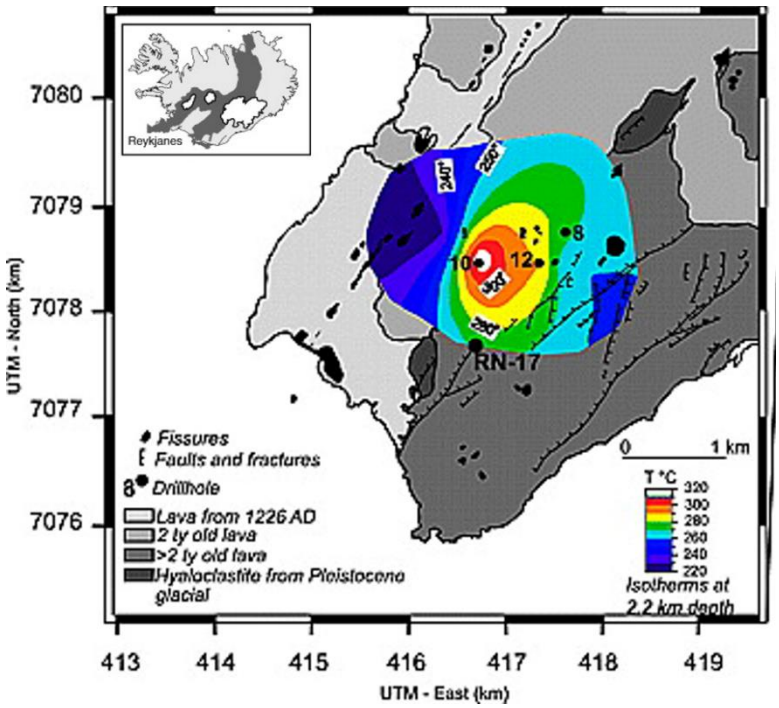

Figure 1. Location and geologic overview of Reykjanes geothermal field. Figure includes locations of four select wells. Figure adapted from (Marks et al. 2011)

2. Geologic Setting

The Reykjanes field is a seawater dominated geothermal system, situated in the tectonically active Reykjanes Peninsula consisting of hyaloclastites interbeded with shallow marine sediments down to about 1km, below which are pillow basalts and basaltic intrusive units (Friðleifsson & Richter, 2010). These are capped by Holocene fissure eruptions of basaltic lavas, the most recent from 1226 AD (Franzson et al., 2002; Friðleifsson, Sigurdsson, et al., 2013). Heat flow to the system is 130 ± 16 MW and is likely provided by a dike network intruded at depth (Fridriksson et al., 2006).

Multiple studies of drill cuttings from the Reykjanes geothermal wells have revealed much about the rocks hosting the geothermal system, and the alteration

they have undergone as a result of hydrothermal reactions (Franzson et al., 2002; Freedman et al., 2010; Gee, Thirlwall, Taylor, Lowry, & Murton, 1998; Marks, Schiffman, Zierenberg, Franzson, & Friðleifsson, 2010; Marks, Schiffman, & Zierenberg, 2011; Pope et al., 2009). The geology hosting the Reykjanes field is relatively consistent across the system as seen in the vertical distribution of rock types and alteration minerals from well to well (Franzson et al., 2002; Fridleifsson & Elders, 2005; Marks, Schiffman, Zierenberg, Franzson, et al., 2010; Pope et al., 2009). These distributions show an alteration zone progressing in alteration intensity with depth as follows: mixed-layer smectite-chlorite, chlorite, mixed-layer clay chlorite – illite, epidote, actinolite, and amphibolite grade alteration (Marks, Schiffman, Zierenberg, Franzson, et al., 2010). This is exemplified by the drill cuttings from well RN-17 described by Marks et al. (2010). Of particular value to the current study is that Marks et al. (2010) report mineral assemblages likely in equilibrium with the fluid from which they formed as indicated by grain inter-growth textures (Table 1) thus allowing interpretation and evaluation of fluid modeling results with direct observations.

Phase separation of steam and liquid, along with decreases in pressure and temperature as the fluids rise from depth during production, cause scale minerals to precipitate in the wellbore and surface pipes (Hardardóttir et al., 2010). Scale minerals collected from within surface pipes of RN-12, RN-21, and RN-24 consist of sphalerite, wurtzite, chalcopyrite, bornite, digenite, and galena, and trace pyrite, and

Table 1. Compiled equilibrium mineral assemblages as reported by Marks et al (2010). The depth of shallowest occurrence and the precipitation type for mineral assemblage are specified when known. Type abbreviations: alt=alteration, am=amygdale, v=vein

Average Depth	**Type**	**Mineral Assemblage**
370	am	chlorite-calcite-pyrite-epidote-wollastonite
	v	wollastonite-quartz
380	v	sphalerite-pyrite-calcite
	v	quartz-pyrite-sphalerite
	am	chlorite-smectite
400	alt	calcite-quartz-chlorite-epidote-pyrite
	alt	pyrite-pyrrhotite-marccasite-sphalerite-galena-quartz-epidote
520	am	Temporal relationship 1st-5th: chlorite, prehnite, epidote, garnet and titanite
720		sphalerite-quartz-prehnite-pyrite-chlorite-epidote
1210		andradite-actinolite
		chlorite-epidote-garnet-quartz
		quartz-epidote-wollastonite-prehnite
1430		amphibole-chlorite-epidote-quartz-anhydrite-wairakite
	am	quartz-chlorite-wollastonite-pyrite-epidote-actinolite-garnet
1800	v	hydrothermal clinopyroxene
2300	v	hydrothermal clinopyroxene epidote, +- anorthite
2300	alt	talc-Fe-oxide- titanite
2260	am	quartz-epidote-pyrite
2866	am	epidote quartz titanite pyrite

pyrrhotite, and amorphous silica (Hardardóttir, Ármannsson, & Þórhallsson, 2005; Hardardóttir et al., 2010). At the wellhead, the only scale minerals found are chalcopyrite, sphalerite, and wurtzite with trace galena. The rest occur after depressurization due to throttling downstream of the wellhead.

A recent study of scale collected from within the wellbores of RN-17b and RN-22 reveal varying proportions of the same minerals listed above for the wellhead, but also include hematite and goethite (Hardardóttir, Hannington, & Hedenquist, 2013). The observation of these minerals precipitating from the Reykjanes geothermal fluid both in the surface pipes and within the wellbore suggest that they must be supersaturated with the fluid and provides another valuable constraint when evaluating modeling results.

3. Well Details

The current study focuses on geothermal well RN-12 located in the Reykjanes field (Figure 1). The well was brought online in May, 2006 as part of a group of wells to feed the then-new 100MW power plant (Fridriksson, Oladottir, & Jonsson, 2010; Sigurdsson, 2010) and for which, production from the system was increased from 50 kg/s to 800kg/s (Fridriksson et al., 2010).

Well RN-12 was drilled in 2002 to a depth of 2506m and cased to a depth of 842m (Rutagarama, 2012). RN-12 has a maximum temperature of 310°C measured at the bottom of the well as shown in the temperature profiles of Figure 2. From observed jogs in the measured temperature profiles, three feed zones are inferred for RN-12 at the following depths below the wellhead: 1000m, 1300m, and 2200m

(Rutagarama, 2012). Well RN-12 produces a two-phase fluid at about 230°C at the wellhead, and has a flashpoint of about 295°C.

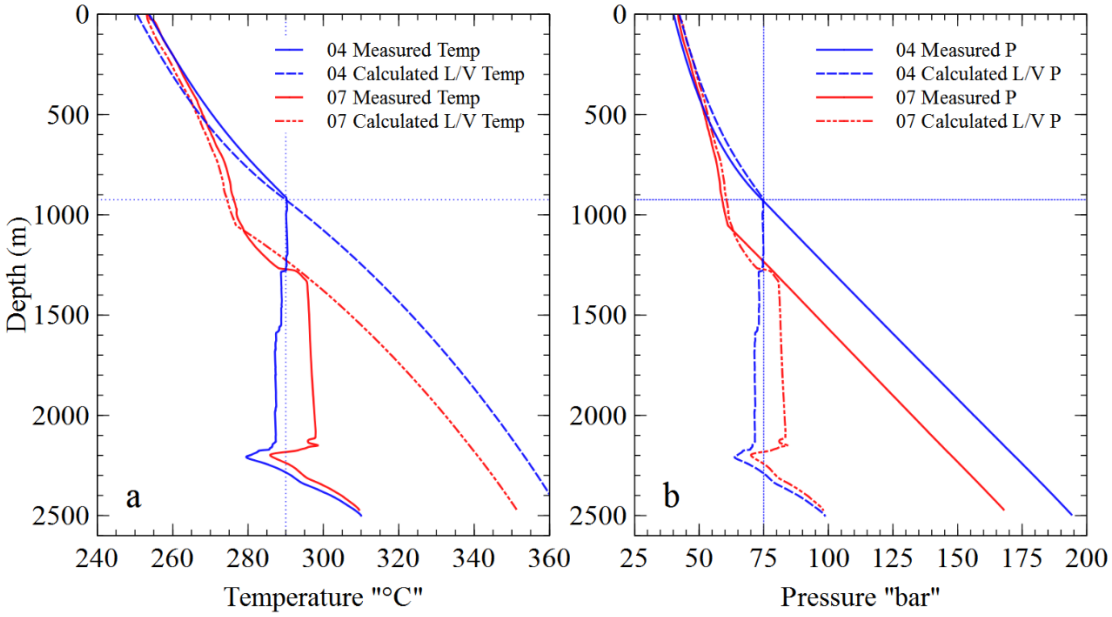

Figure 2. Pressure and temperature profiles for well RN-12. One measured in 2004 with a 40 bar head pressure and flowing 10kg/s, the other from 2007 with a closed wellhead pressure of 42 bar. Graph (a). Measured temperature curves are plotted along with calculated temperature. Curves are calculated with IAPWS-IF97 standards for the liquid-vapor curve based on the measured temperature in P-T profile. Point of deviation between curves is the flash point location (b) Correlative plot to "a" showing measured and calculated pressures.

4. Fluid Samples

Two sample types are compared in the current study. The first are downhole samples collected below the depth of boiling with a mechanical sampler developed and deployed by Kevin Brown (Hardardóttir et al., 2009). Three downhole samples were retrieved from the Reykjanes system in May 2007, one each from wells RN-12, RN-19, and RN-21, for which analytical results are given in Table 2 (Hardardóttir et al., 2009).

Table 2. Downhole sample analysis converted to molality from (Hardardóttir et al., 2009).

Well	RN-12DH	RN-19DH	RN-21DH
Sample #	20070092	20070089	20070086
Date Collected	5/9/2007	5/7/2007	5/1/2007
Aqueous Species (molality)			
H+	NA	NA	NA
H2O	1kg	1kg	1kg
Cl[a]	5.24E-01	5.11E-01	5.28E-01
SO4	NA	NA	NA
CO2	NA	NA	NA
H2S	NA	NA	NA
SiO2	1.00E-02	1.10E-02	1.10E-02
Al	1.01E-04	1.50E-05	5.00E-05
Ca	4.70E-02	4.32E-02	4.40E-02
Mg	3.90E-04	8.00E-05	1.70E-04
Fe	4.30E-04	1.54E-04	2.43E-03
K	3.80E-02	3.80E-02	4.10E-02
Na	3.93E-01	3.89E-01	3.97E-01
Mn	5.20E-05	3.76E-05	4.90E-05
Zn	3.93E-04	7.90E-05	1.89E-04
Cu	2.61E-04	2.08E-04	2.07E-04
Pb	1.30E-06	6.00E-07	1.40E-06
F	NA	NA	NA
As	1.50E-06	1.50E-06	2.00E-06
NH4+	NA	NA	NA
H3BO3	7.09E-04	7.15E-04	6.84E-04

[a] Value was not measured but calculated from NA, K, Ca (Hardardottir et al. 2009)

The downhole samples were collected below the boiling depth in the wells to sample the single-phase fluid before phase separation occurs. The chemical analyses as reported by Hardardottir et al. (2009) do not include species affected by loss of dissolved gasses with depressurization of the sample chamber: H^+, H_2S, SO_4, and CO_2. Without gas data, calculations of pH and distributions of species are not meaningful. Thus, the use of equilibrium calculations for evaluation of the downhole sampling results alone is not possible.

The second sample type consists of fluid and gas samples collected at the wellhead by Iceland GeoSurvey under contract with HS Orca. Wellhead samples of liquid and steam were taken using a Webre separator and a 'Giggenbach Bottle' for the gases, as explained by Arnorsson et al. (2006). These samples are analyzed individually and the original fluid is reconstructed to represent the fluids at depth before boiling. The method of reconstruction is discussed in CHAPTER III. SEC 3.

Samples have been collected from Well RN-12 approximately biannually since its construction in 2003 by the Icelandic GeoSurvey, ISOR, under contract with the geothermal company, HS Orca. Twenty samples of liquid and vapor were collected from the well between 2003 and 2012, of which nine were selected for use in this study, and are presented in the APPENDIX. Samples were rejected from the study if an analysis contained, missing components or one or more erroneous values.

CHAPTER III
MODELING METHODS

1. Application of Classical Equilibrium Theory

Owing to the lack of dissolved gas data in the downhole samples and the wellhead samples being two-phase fluids, their sample analyses cannot be compared directly but one or the other must be adjusted so the physical states of each are equal. For this study, classical thermodynamic modeling will be applied to fluid sample analyses to allow the effects caused by changing pressure and temperature on the chemical state of the fluid to be explored.

If only thermodynamic equilibrium is invoked, the composition of the reservoir fluid from which the fluids at the wellhead originate is a result of five effects acting on it: temperature, pressure, the composition and amount of rocks it is in contact with, and the fluid's composition before coming in contact with these rocks. If any of these change, so also will the composition of the fluid change, until a new equilibrium state is reached. By this reasoning, the use of wellhead fluid samples to understand the reservoir fluid composition would be impossible without also knowing the amount and composition of every mineral that the fluid has come into contact with, in addition to the pressure and temperature conditions along its flow path.

Yet it is not only equilibrium that controls the evolution of geothermal fluid composition but also the time over which a chemical reaction takes place. The degree that the fluid will interact with its surroundings will range corresponding to

this interplay between rates of fluid flow, reaction kinetics, diffusion of dissolved species, and thermodynamic equilibrium. Thus by also considering kinetic controls on when and where stable, metastable, and dis-equilibrium conditions exist over a fluid's evolution, equilibrium modeling results can be used to tease out the history of reactions a fluid has experienced since its last stable equilibrium composition. This requires a framework to understand the relationship between fluid flow and equilibrium modeling and is considered for well RN-12 in the following paragraphs.

A fluid will continue to "adjust" to its surroundings to stay in complete thermal and chemical equilibrium until fluid flow velocity increases. Fluid flow will vary with varying reservoir permeability, and both are generally considered to decrease with depth into the reservoir. If fluid flow velocity is slow before reaching the well, the fluid will reach equilibrium between the rocks it was flowing through. With increased fluid flow rates in the well, the limiting factor on reactions controlling fluid composition will shift from stable equilibrium to reaction kinetics, allowing a combination of metastable and disequilibrium mineral assemblages.

Reaction progress between the fluid and surrounding minerals will be a maximum when equilibrium is reached and minimized to zero when contact time for reactions to occur approaches zero. Thus if fluid flow increases quickly and to a high rate the fluid will no longer be in chemical equilibrium with its surroundings but instead will contain a record of equilibrium for the state of the fluid before the sudden change occurred. In natural geothermal systems reaction progress will never be at ideal end member cases but fall somewhere in between with each mineral's ability to reach equilibrium with the fluid controlled by its reaction rate.

As an example take the relationship of dissolved silica, $SiO_{2\,(aq)}$, concentration in geothermal fluids. When these fluids are in contact with quartz, the $SiO_{2\,(aq)}$ concentration in the fluid will be controlled by the thermodynamic equilibrium for quartz-fluid interaction. When the fluid flow rates increase, so does the rate of change in temperature and pressure felt by the fluid. With increasing flow rates there will be a point when the kinetic reaction rate of quartz precipitation becomes slower than the rate of change in the equilibrium value of $SiO_{2\,(aq)}$ between quartz and the liquid, and the amount of $SiO_{2\,(aq)}$ in the fluid will become oversaturated with respect to quartz. At this point, fluid equilibrium between the two no longer is in control, but instead is under a combination of equilibrium and kinetic controls; the faster the change in physical state felt by the fluid the more emphasized kinetic control becomes.

When the fluid pressure decreases quickly in a geothermal system, as with adiabatic boiling within a geothermal well, the amount of $SiO_{2\,(aq)}$ does not have time to adjust to its new physical state by creating organized quartz crystals but will rather continue to contain its earlier value. Decreasing temperature causes the amount of $SiO_{2\,(aq)}$ needed for equilibrium with quartz and its polymorphs to decrease. If the changing state of the fluid continues in such a way that the temperature and pressure are allowed to decreases enough with $SiO_{2\,(aq)}$ remaining constant, amorphous-silica saturation will be reached, the reaction kinetics of which are significantly faster than for quartz formation, allowing equilibrium to be attained between the fluid and amorphous-silica. As temperature and pressure continue to decrease the concentration of $SiO_{2\,(aq)}$ dissolved in the fluid will also

decrease by precipitating amorphous silica until the equilibrium between amorphous silica and the fluid is reached.

At temperatures relevant to the Reykjanes field, 200 to 350°C, quartz is the thermodynamically stable mineral, yet amorphous silica is observed as the main scale mineral in well RN-9 where temperatures and pressures were such that amorphous silica saturation was reached (Hardardóttir et al., 2010). The pretense of metastable mineral assemblages illustrates this interplay of control on the chemical composition of the fluid. The slow reaction rates of many minerals such as quartz allow fluids to keep a record of their equilibrium condition before fluid ascent, and thus allow wellhead sampling of geothermal wells to be used to interpret fluids originating at depth. However as suggested above, because of the uncertainty in the relationship between kinetic and equilibrium, this behavior also gives rise to much of the uncertainty in using equilibrium modeling to understand the chemical history of a geothermal system.

2. Pressure and Temperature Logs

Pressure and temperature logs from RN-12 are used to understand the state of the fluid as it exists in the well. Figure 2 reveals the depth of initial boiling within RN-12 as the point of divergence between measured and calculated values of P and T. Calculated curves were created using a Python implementation of the international standard IAPWS-IF97 equations of state for pure water (https://pypi.python.org/pypi/iapws). Data from well logs include measurements of pressure and temperature with depth. The calculated temperature curve was created by finding the required temperature to bring each measured pressure point

to liquid-vapor saturation. In other words, we produced a curve which gives the hypothetical temperature of all measured depths in the well by assuming that liquid and vapor are present at all points. The same approach is used to find the hypothetical pressure curve, by calculation of the pressure required for liquid-vapor saturation at the measured temperature. Where the measured temperature and calculated temperature curves are equal, the fluid must contain water both in its liquid and steam phases.

By using equations of state for pure water, the excess pressure due to dissolved gasses in the fluid and the boiling point elevation of the liquid phase owing to dissolved constituents is not taken into account (Driesner & Heinrich, 2007). These factors should be included to increase the accuracy of curves, but the pure fluid assumption used here provides a close approximation to real world behavior.

3. Wellhead Fluid Reconstruction Methods

The concentration reported in downhole sample analyses is interpreted as a direct representation of the single phase fluid at depth because it was directly sampled as such, but the wellhead sample is collected after the fluid has boiled, necessitating that it be reconstructed to represent the pre-boiled fluid. This is done by deducing the correct amount of sampled steam that should be combined with the sampled liquid. The ratio by weight of steam in the total two phase discharge, steam fraction, at the sampling location was determined by assuming adiabatic flow within the well and setting the initial boiling temperature within the well to 290°C , or 295°C as observed from pressure and temperature logs.

By approximating fluid flow as adiabatic, boiling within the system is defined to be isenthalpic, which by definition sets the specific enthalpy per unit mass of fluid to a constant value, H_{dh}^{L}. Setting the initial boiling temperature to 295°C sets the constant enthalpy of boiling to the enthalpy of the liquid phase at the flash point temperature, 1317 kJ/kg (IAPWS-IF97). The assumption of adiabatic flow dictates that no heat is gained or lost between the fluid and the walls of the well, therefore the temperature decrease with boiling can be fully described by the energy used in vaporization.

The weight fraction of steam in the two phase fluid, X, at the wellhead is found using Equation (1):

$$X = \frac{H_{dh}^{L} - H_{wh}^{L}}{H_{wh}^{V} - H_{wh}^{L}} \qquad (1)$$

The measured pressure at the wellhead during fluid sampling sets the enthalpy of the wellhead liquid, H_{wh}^{L}, and vapor, H_{wh}^{L}, phases. Applying these calculations to a well requires justification of some assumptions: the two separate phases must be traveling at the same velocity and come from the same source. Thus if mixing of fluids containing different enthalpies occurs the reconstruction will be in error.

4. Equilibrium Calculations

Multicomponent equilibrium calculations are executed with programs SOLVEQ-XPT, and CHIM-XPT (a revision of CHILLER). SOLVEQ-XPT is used for calculations of equilibrium of the aqueous phase alone, and CHIM-XPT is for

calculations of multi-phase equilibrium, involving the aqueous phase and if calculated to be present, a gas or any mineral phases in the system (Reed, 1998). Both programs rely on SOLTHERM.XPT (http://pages.uoregon.edu/palandri/data/soltherm.xpt) a thermodynamic database containing equilibrium constants for aqueous, gas, and mineral species. Most equilibrium constants are computed using SUPCRT92 (Johnson, Oelkers, & Helgeson, 1992), with mineral data from Holland and Powell (1998) for silicates, oxides, hydroxides, and carbonates and data for sulfide mineral and aqueous species from SLOP.98 (Shock & Helgeson, 1988; Shock, Sassani, Willis, & Sverjensky, 1997).

4.1. Program SOLVEQ-XPT

Saturation diagrams are created using program SOLVEQ-XPT on a fluid composition to calculate a distribution of species for a range of temperatures and corresponding liquid-vapor pressures (Palandri & Reed, 2001; Pang & Reed, 1998; Reed & Spycher, 1984). At each temperature the saturation indices, log Q/K, of all minerals derivable from the starting component species are calculated based on the distribution of aqueous species. A value near zero indicates that the mineral is saturated, in equilibrium, with the aqueous phase. A mineral is undersaturated if log Q/K is negative, and supersaturated if positive.

The temperature where multiple mineral saturation values converge on a Log Q/K of zero indicates the temperature at which the fluid was in equilibrium with the minerals involved. This convergence is used here, as documented by previous workers, to tease out the mineral assemblage and the temperature when fluid were in stable, or metastable equilibrium at depth before being sampled at the

wellhead(Reed, Spycher, & Palandri, 2010; Reed & Spycher, 1984). Convergence of log Q/K curves of natural waters is rarely perfect for a number of reasons, such as the following: choosing minerals not in the equilibrium assemblage at depth, lagging mineral precipitation due to kinetic effects or, sampling and thermodynamic database errors (Palandri & Reed, 2001). Consequently, minerals that fall just above or below saturation at the convergence temperature need to be considered and evaluated on a case-by-case basis.

In addition to using mineral saturation diagrams to determine the temperature and equilibrium mineral assemblage of the reconstructed fluid, we apply saturation calculations to the sample analysis of the pure-liquid phase at the wellhead. This allows the accuracy of the analysis to be evaluated and to gain awareness for which minerals are precipitating as scale within the wellbore. Applying these calculations to the liquid-phase alone without first accounting for the corresponding vapor phase is a significant deviation from their traditional use as described above.

The application of saturation diagrams to the liquid component of a two-phase fluid only has physical meaning at the temperature and pressure condition of sampling, and therefore has no direct predictive ability for other conditions without outside information. What it does allow is equilibrium modeling of the aqueous fluid under a set of measured conditions, with well-defined model inputs. Therefore, we are able to estimate the degree to which equilibrium is reached within the aqueous phase as part of a multiphase fluid flowing through the wellhead as discussed in CHAPTER IV. SEC 1.2

Mineral saturation indices are calculated over a range of temperatures, and for all minerals that can be constructed out of the components given as input to SOLVEQ-XPT and contained in the SOLTHERM database of almost five hundred minerals. However, most of these do not apply to the system being studied and can be immediately refined to possible minerals by throwing out minerals that are calculated to be highly, over, and undersaturated throughout the temperature range. These minerals are then evaluated further by considering those that show up in the well cuttings and well scale summarized in Table 1.

Solid Solutions in SOLVEQ-XPT

A previous limitation to calculations of mineral saturation with SOLVEQ-XPT was the lack of treatment for solid solutions, because only end member mineral compositions were computed. To address this, selected solid solution saturation indices have been calculated for the most stable solid solution compositions assuming binary-multisite-ideal mixing between end members.

Saturation indices for solid solutions are computed using classic thermodynamic theory of binary ideal mixtures. This treatment is conceptualized next, starting from the process of Gibbs Free Energy minimization.

A chemical reaction is spontaneous if the change in Gibbs Free Energy for a reaction, $\Delta_r G$, is negative, and if codependent reactions are defined, then the reaction with the most negative change in Gibbs Energy will be favored. The change in Gibbs Free Energy for a reaction is found by calculating the reaction's effect from

a standard state for which the change in Gibbs Energy can be found, the standard Gibbs Free Energy of reaction, $\Delta_r G°$:

$$\Delta_r G = \Delta_r G° + RT \ln Q \quad (2)$$

The activity quotient, Q, in equation (2) is the product of all activities, a_i involved in a reaction, each raised to the power of their stoichiometric coefficient,v_i.

$$v_a A + v_a B \Leftrightarrow v_a C + v_a D \quad (3)$$

$$Q = \frac{a_C^{v_c} a_D^{v_d}}{a_A^{v_a} a_B^{v_b}} \quad (4)$$

When expanded to the general case, v_i for reactants is defined as negative allowing Q to be written as follows:

$$Q = \prod_i a_i^{v_i} \quad (5)$$

When a reaction reaches equilibrium, the Gibbs Free Energies of the products and of the reactants are equal. Thus, at equilibrium, the change in Gibbs Free Energy of reaction becomes zero allowing equation (2) to be simplified to equation (6), and Q become the equilibrium constant, K.

$$\Delta_r G° = -RT \ln K \quad (6)$$

The equilibrium constant, K, does not have theoretical meaning outside of equilibrium. However, its use as stable point to which Q can be compared allows the degree and direction a reaction is from its equilibrium state to be quantified. This can be taken a bit farther by combining equations (2) and (6):

$$\Delta_r G - [-RT\ ln\ K] = RT\ ln\ Q \quad (7)$$

$$\Delta_r G = RT ln \frac{Q}{K} \quad (8)$$

At equilibrium, Q is equal to K, causing $\Delta_r G$ to be zero. With Q greater then K, $\Delta_r G$ is greater than zero suggesting that the reaction as written will proceed to the left. Lastly, having Q less than K will cause $\Delta_r G$ to be negative, shifting the reaction to the right.

The total change in Gibbs Free Energy, $\Delta_r G^{\circ}_{SS}$, for a solid solution,

$$\Delta_r G^{\circ}_{SS} = \sum_j \left[x_i\ \Delta_r G^{\circ}_j\right] + \Delta_{mix} G \quad (9)$$

is calculated by adding the change from each end member's standard Gibbs Free Energy of reaction, $\Delta_r G^{\circ}_j$. Each end members contribution is determined by its mole fraction, x_i, in the solid solution. The free energy change from each end member is then reduced further due to the change in Gibbs Free Energy as a result of ideal mixing, $\Delta_{mix} G$.

In solid solutions, the free energy of mixing must be calculated for the number of mixing sites, *n*, per formula unit of the solid solution of interest. For example, ferric iron and aluminum can exchange on 2 octahedral mixing sites in garnet to make end members grossular and andradite. While other end members could also be included, solid solutions were limited to binary mixing such that the solid solution composition can be described by the mole fraction of two end members to increase computational efficiency. This site in garnet can contain Ca^{2+}, Mg^{2+}, Mn^{2+}, and Fe^{2+} (Anderson, 2008), but in the Reykjanes geothermal fluids, the concentration of Ca^{2+} is 2 orders of magnitude greater than the others added

together. This causes grossular and andradite to dominate the composition of garnet calculated to be in equilibrium with the Reykjanes fluid thus making the binary system a good approximation of the system.

The free energy change of ideal mixing, $\Delta_{\mathrm{mix}}\mathrm{G}$, is due to an increase in entropy for solutions as described from the second law of thermodynamics to take the form of equation (10).

$$\Delta_{mix}G = T\Delta S \tag{10}$$

Where T is temperature in Kelvin, and ΔS is the change in entropy. By constraining mixing to ideal, Gibbs Free Energy is equal to the negative change in entropy scaled with temperature. When equation (10) is expressed with statistical mechanics, $\Delta_{\mathrm{mix}}\mathrm{G}$, takes the form of equation (11):

$$\Delta_{mix}G = -nRT\sum_{j} x_j\, ln(x_j) \tag{11}$$

Combining equations, (6), (9), and (11) with the assumptions of ideal mixing and constant pressure, temperature, and volume, yields the following equation:

$$\Delta_r G^{\circ}_{SS} = -RT\sum_{j}[x_j\ \ ln\, K_j] + n\sum_{j} x_j\, ln\, x_j \tag{12}$$

Where:

R = *The universal gas constant*

T = *Temperature*

n = *number of mixing sites*

K = *Equilibrium constant for end member* (j)

x = *Mole fraction of end member* (j)

The Gibbs Free Energy of Reaction for the solid solution can also be written in the form of equation (6), and combined with equation (12) to solve for ln K_{SS}.

$$\Delta_r G_{SS}^{\circ} = -RT\ ln(K_{SS}) \tag{13}$$

$$ln\ K_{SS} = \sum_j \left[x_j\ ln\ K_j\right] - n \sum_j x_j\ ln\ x_j \tag{14}$$

To define the solid solution saturation index, equation (14) can be related to Q at the current state to get $ln\frac{Q_{SS}}{K_{SS}}$:

$$ln\frac{Q_{SS}}{K_{SS}} = ln\ Q_{SS} - \left[\sum_j \left[x_j\ ln\ K_j\right] - n \sum_j x_j\ ln\ x_j\right] \tag{15}$$

The solid solution activity quotient, Q_{SS}, is computed by using activities for all involved aqueous species in equation (5), but because SOLVEQ-XPT already solves Q for solid solution end members, they can be used to find Q_{SS} directly by knowing the mole fraction of each end member involved. This can be shown using an example of solid solution replacement, between elements B, and C in a simplified mineral, $A(B,C)_v$ as follows:

$$AC_v \Leftrightarrow A + vC \tag{16}$$

$$AB_v \Leftrightarrow A + vB \tag{17}$$

$$A\left(B_{v\,x_b}, C_{v\,x_c}\right) \Leftrightarrow A + (v\,x_c)C + (v\,x_b)B \tag{18}$$

$$A\left(B_{v*x_b}, C_{v*x_c}\right) \Leftrightarrow x_b AB_v + x_c AC_v \tag{19}$$

$$x_b AB_v + x_c AC_v \Leftrightarrow A + (v\,x_c)C + (v\,x_b)B \tag{20}$$

$$x_b + x_c = 1 \tag{21}$$

Where x_b and x_c are the mole fraction of each end member of the solid solution and add to one. The solid solution activity quotients can then be found from each end member:

$$Q_{AC} = \frac{a[A]a[C]^v}{a[AC_v]} \tag{22}$$

$$Q_{AB} = \frac{a[A]a[C]^v}{a[AC_v]} \tag{23}$$

$$Q_{SS} = \frac{a[A]\ a[B]^{(v\,x_b)}a[C]^{(v\,x_c)}}{a[AB_v]^{x_b}\ a[AC_v]^{x_c}} = \left(\frac{a[A]a[A]^v}{a[AB_v]}\right)^{x_b}\left(\frac{a[A]a[C]^v}{a[AC_v]}\right)^{x_c} \tag{24}$$

$${Q_{AB}}^{x_b}{Q_{AC}}^{x_c} = \left(\frac{a[A]a[A]^v}{a[AB_v]}\right)^{x_b}\left(\frac{a[A]a[C]^v}{a[AC_v]}\right)^{x_c} \tag{25}$$

$$Q_{SS} = {Q_{AB}}^{x_b}{Q_{AC}}^{x_c} \tag{26}$$

$$Q_{SS} = \prod_j {Q_j}^{x_j} \tag{27}$$

$$ln\, Q_{SS} = \sum_j [x_j\ ln\, Q_j] \tag{28}$$

The relationship in equation (28) used in equation (15) gives the saturation index in natural log form for the solid solution for any end member composition:

$$ln\frac{Q_{SS}}{K_{SS}} = \sum_j [x_j\ ln\ Q_j] - \sum_j [x_j\ ln\ K_j] - n\sum_j [x_j\ ln\ x_j] \quad (29)$$

A solid solution saturation index in Log base 10, as defined in SOLVEQ-XPT, can be found directly from the saturation indices output from SOLVEQ-XPT by rearranging Equation (29) and converting between logarithm bases.

$$ln\frac{Q_{SS}}{K_{SS}} = \sum_j \left(x_j ln\frac{Q_j}{K_j} - n\,x_j ln\,x_j\right) \quad (30)$$

$$\frac{log\frac{Q_{SS}}{K_{SS}}}{log(e)} = \sum_j \left(x_j\frac{log\frac{Q_j}{K_j}}{log(e)} - \frac{n\,x_j\,log\,x_j}{log(e)}\right) \quad (31)$$

$$log\frac{Q_{SS}}{K_{SS}} = \sum_j \left(x_j\,log\frac{Q_j}{K_j} - n\,x_j\,log\,x_j\right) \quad (32)$$

The form of equation (32) gives the solid solution saturation index of any one composition defined by the mole fractions of its end members.

For codependent reactions, the one that lowers the Gibbs Free Energy the greatest will be favored. Every mineral formation reaction in SOLTHERM is written as a dissolution reaction, with the mineral on the left. This means that if Gibbs Free Energy is negative, the mineral will dissolve, and if positive, the mineral will precipitate.

Therefore, the most stable solid solution composition will be the one that maximizes the positive change in Gibbs Free Energy. Using the relationship between saturation index and Gibbs Free Energy of reaction from equation (8) this principle can also be applied to the saturation index. The composition with the largest saturation index will be the thermodynamically favored composition to precipitate.

For each temperature where a distribution of species is calculated with SOLVEQ-XPT, one ideal solid solution composition and saturation index for that temperature is selected by iterating equation (32) over the mole fraction of end members and finding the maximum.

4.2. Program CHIM-XPT

To move beyond single phase modeling, program CHIM-XPT is used to calculate equilibrium among not only the aqueous species, but also with any mineral and gas phases calculated to be present in the system as described in Reed (1998). Calculations for the saturation state of minerals and gases are calculated in SOLVEQ-XPT and reported as over or undersaturated. In program CHIM-XPT, if a mineral is found to be oversaturated in the aqueous phase, its component species can be stoichiometrically shifted to the solid phase.

To find the maximum concentrations of dissolved species, CHIM-XPT is used to computationally re-dissolve minerals that precipitate as scale in the well on ascent to the wellhead. The maximum amount of a mineral that can dissolve depends on its solubility in the fluid as defined by its thermodynamic properties. For our purpose here, mineral titration in CHIM-XPT is done by iteratively adding the components of the dissolving mineral while suppressing all other minerals calculated to precipitate before saturation with the dissolving mineral is reached. Suppressing minerals is done to find the maximum value between the forced mineral and the fluid reconstruction but means the sample is not in stable equilibrium, but is forced into a metastable equilibrium. The choice of minerals for

this study was determined from minerals observed to precipitate as scale in the Reykjanes system as described in section CHAPTER II. SEC 2.

CHAPTER IV
RESULTS AND MODELING DISCUSSION

1. Wellhead Samples

Ideally, for a reconstructed wellhead fluid to represent the reservoir fluid, the fluid will have reached stable equilibrium at depth before the fluid is quickly brought to the surface. Therefore, the fluid would carry its exact composition from depth to the surface without change. However, natural geological systems are shifted from ideal due to scale mineral precipitation within the well and incomplete equilibrium at depth. Knowing the composition of scale minerals allows their effect on the wellhead fluid to be accounted for, and by tracking the change in modeled fluid equilibrium for wellhead reconstructions through time, the shifts from ideal because of non-equilibrium within the reservoir can be understood.

Mineral saturation diagrams for wellhead fluid samples of RN-12 from 2004, 2006, 2008, 2010, and 2012 are shown in Figure 3. For each year's analysis, the state of mineral saturation was modeled in two ways: (a) the analysis of the liquid alone is used to model the chemistry at the P and T of sampling (graphs on left), and (b) the reconstructed fluid, accounting for both steam and liquid, is used to investigate the conditions in the reservoir (graphs on right).

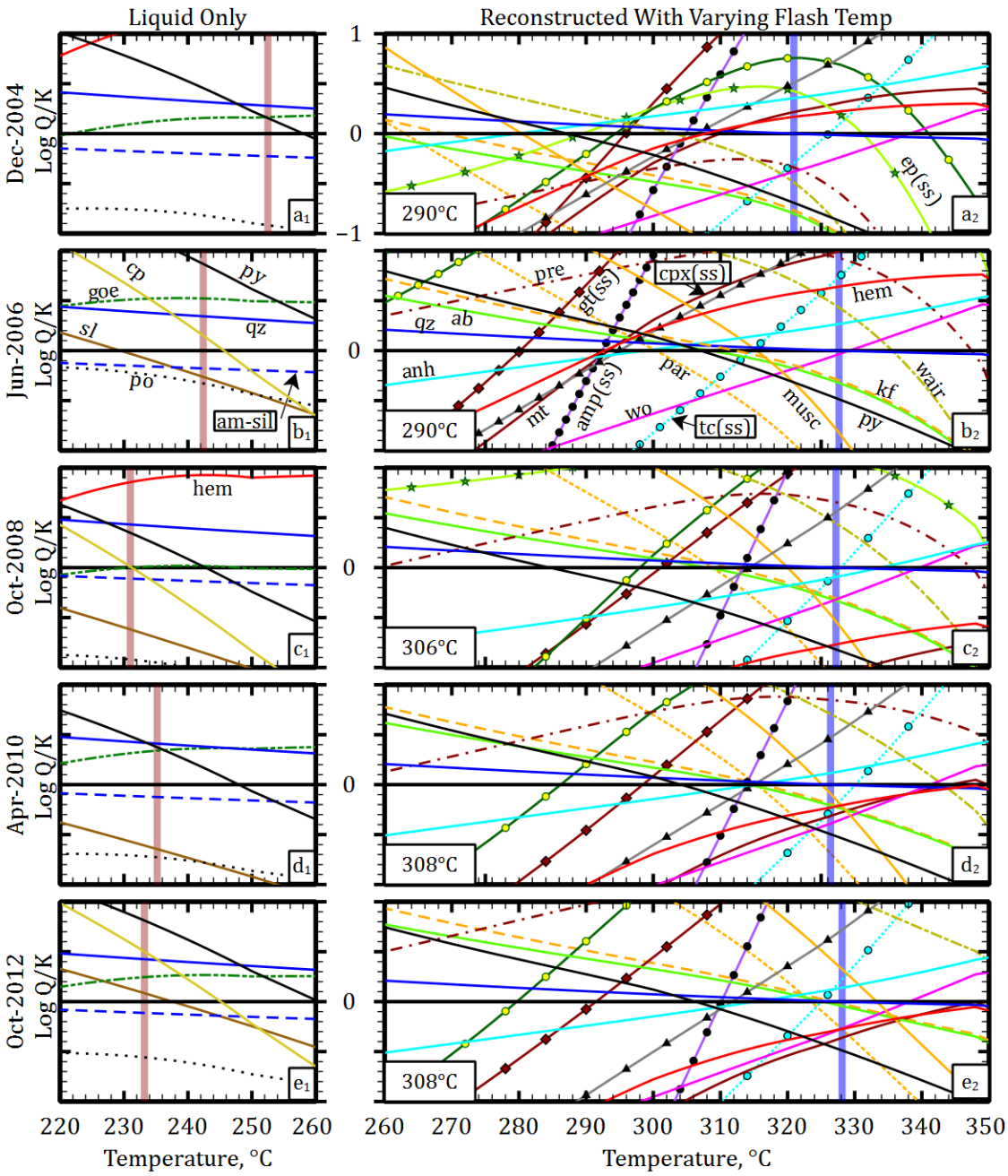

Figure 3. Mineral saturation diagrams for well RN-12 from 2004 to 2012. Graphs (a_1-e_1) are diagrams for the liquid phase only at the sampling location. Red vertical lines highlight the temperature of samplings for each sample. Graphs (a_2-e_2) are for reconstructed fluids according to the best estimate of initial boiling temperature for each sample, (specified in lower left of each graph). In each graph, the temperature where quartz is exactly saturated is marked by a vertical blue bar. The vertical scale for all samples is equal, ranging from 1 to -1 log Q/K. Mineral abbreviations are shown in Table 3.

Table 3. Mineral Abbreviations

ab	albite	hd	hendenbergite
amp	amphibole	hem	hematite
am-sil	amorphous silica	kf	K-feldspar
anh	anhydrite	mt	magnetite
chl	chlorite	musc	muscovite
clinoc	clinochlore	par	paragonite
clinoz	clinozoisite	po	pyrrhotite
cp	chalcopyrite	pre	prehnite
cpx	clinopyroxene	py	pyrite
daph	daphnite	qz	quartz
di	diopside	sl	sphalerite
ep	epidote	tc	talc
goe	goethite	wair	wairakite
Gt	garnet	wo	wollastonite
gn	galena		

RN-12 was drilled in 2002 and kept offline until its utilization for production started in May, 2006 (Rutagarama, 2012). To feed a new power plant in 2006 the total production of the Reykjanes geothermal field was increased from 50 kg/s to 800kg/s (Fridriksson et al., 2010). The samples used in Figure 3 graphs (a_1) and (a_2) were collected May 25, 2004, over a year after the well was drilled but before production from RN-12 began. The samples used in graphs (b_1) and (b_2) were collected June 14, 2006, about a month after production began. The time progression in Figure 3 is referred to throughout the following sections to illustrate the effects of sustained flow out of the system on fluid equilibrium, and to give temporal context to the relationship between the downhole sample and wellhead samples.

1.1. Wellhead Fluid Reconstruction

Wellhead samples of liquid and steam from RN-12 were reconstructed to represent the reservoir fluid using an enthalpy based on the temperature of initial boiling, as explained in CHAPTER III. Mineral saturation diagrams for these reconstructions are shown in Figure 3, graphs (a_2-e_2). For each sample reconstruction, the boiling point assumed was allowed to vary. Estimates of initial boiling within the well during the 2004 and 2006 samplings are determined using the 2004 pressure and temperature logs in Figure 2. Wellhead enthalpy was measured by ISOR in 2011 with flow tracers to be 1390kJ/kg (T. Fridleifsson, pers. commun. 2013), corresponding to a boiling point temperature of 308°C, and was used to reconstruct the 2010 and 2012 sampled fluids. The flash point of the 2008 sample reconstruction was initially set to 295°C as indicated by the temperature log from 2007, but after finding the consistency in the temperature of quartz saturation, the flash point assumption was changed to 306°C (graph c_2) to bring its quartz temperature into the same range as other samples. The consistency in the temperature of quartz saturation between wellhead reconstructions through time suggest that the quartz temperature is being set by fluid-quartz equilibrium within the reservoir and not by the changing flash point temperature, or the variable wellhead pressure.

The reconstructed fluid from 2006, (graph b_2), is in equilibrium with quartz and wollastonite at a temperature of about 330°C. However, at a temperature of 292°C, the fluid is calculated to be in equilibrium with the following mineral assemblage: anhydrite, hematite, magnetite, paragonite, and amphibole and

pyroxene solid solutions. Of these minerals, all but paragonite are seen in drill cuttings of the Reykjanes system, but if there was time for these minerals to reach equilibrium, quartz also should be in the equilibrium assemblage. This suggests that our calculations for quartz saturation are in error, and the true quartz saturation temperature is likely 292°C as well. The temperature of quartz saturation is very sensitive to small changes in the dissolved silica concentration due to the very shallow slope of the quartz saturation curve relative to other minerals. The consistency between quartz temperatures from year to year as shown in Figure 3, suggest accuracy in the measured analysis and indicates a systematic error in the calculation of quartz saturation indices.

In addition to calculating the fluid's saturation state with minerals, ideal solid solution compositions were determined by calculating the ideal composition that minimizes Gibbs Free Energy, as explained in CHAPTER III. The same solid solution saturation indices plotted for the 2006 wellhead sample in Figure 3, graph (b_2), are highlighted in Figure 4, graph (a). On graph (b), the corresponding solid solution compositions are plotted as a function of temperature. Therefore, at any given temperature in Figure 4 there is one thermodynamically favored composition for each solid solution. Thus, by knowing the composition of a solid solution presumed to be in equilibrium with the reservoir fluid, the temperature of equilibrium between the two can be estimated.

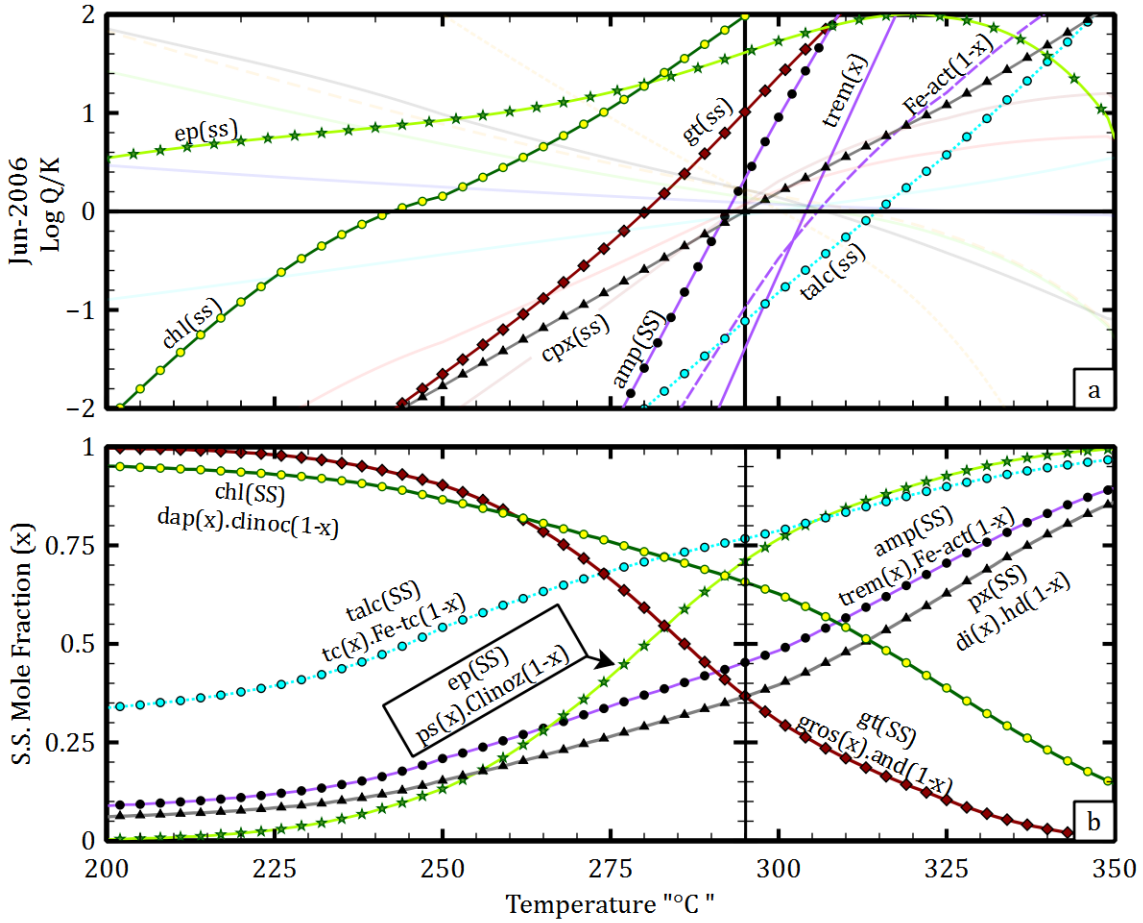

Figure 4. Solid solution saturation diagram for 2006 wellhead sample. Graph (a) highlights solid solution saturation curves from Figure 3, graph (b_2), with the addition of amphibole solid solution end members, tremolite, and Fe-actenolite. Graph (b) end member compositions that maximize log Q/K, by minimize Gibbs Free Energy for each solid solution in graph (a). Mineral abbreviations are shown in Table 3.

Solid solution compositions from RN-17 drill cuttings (Marks, Schiffman, Zierenberg, Franzson, et al., 2010) are used here to estimate the range for solid solutions in equilibrium with the RN-12 reservoir fluid. These are shown in Table 4, along with a calculated temperature range for each. This temperature range is determined by matching the upper and lower solid solution compositions from drill cuttings with the composition-temperature curves in Figure 4.

Table 4. Range in solid solution compositions from drill cutting of RN-17, (Marks, Schiffman, Zierenberg, Franzson, et al., 2010), and the corresponding temperature range using ideal composition calculated from 2006 wellhead reconstruction, Figure 4.

SS Composition	Drill cutting Range *x*	Figure 4 Temp range
Chlorite: $dap_x,clinoc_{1-x}$	0.45 - 0.71	319°C – 285°C
Epidote: $ps_x,clinox_{1-x}$	0.16 - .47	252°C - 277°C
Garnet: $gros_x,and_{1-x}$	0.38 – 0.5	295°C - 286°C
Amphibole: $trem_x,Fe\text{-}act_{1-x}$	0.5 – 0.7	302°C - 324°C
Pyroxene: di_x,hd_{1-x}	.05 - .7	200°C - 332°C

With the exception of the calculated upper temperature of 277°C for epidote, the temperature range of all other solid solutions from the drill cutting overlap with the estimated temperature range of 290°C – 310°C for the reservoir fluid. Thus, the good temperature correlation adds validity to the reconstructed fluid composition and in using ideal multisite mixing to calculate solid solution saturation curves. However, by accounting for non-ideality in solid solution mixing calculations, the usefulness of this method can likely be increased.

To explore the effect of varying enthalpy, mineral saturation plots were calculated for the 2006 sample at five wellhead enthalpy assumptions from 1290kJ/kg to 1594kJ/kg (Figure 5). The two extreme enthalpies correlate to fluid flash point temperatures within the well of 290°C and 340°C respectively if adiabatic fluid flow is assumed. Graph (a) corresponds to the reconstruction used in the above discussions, where a wellhead enthalpy of 1290kJ/kg was assumed.

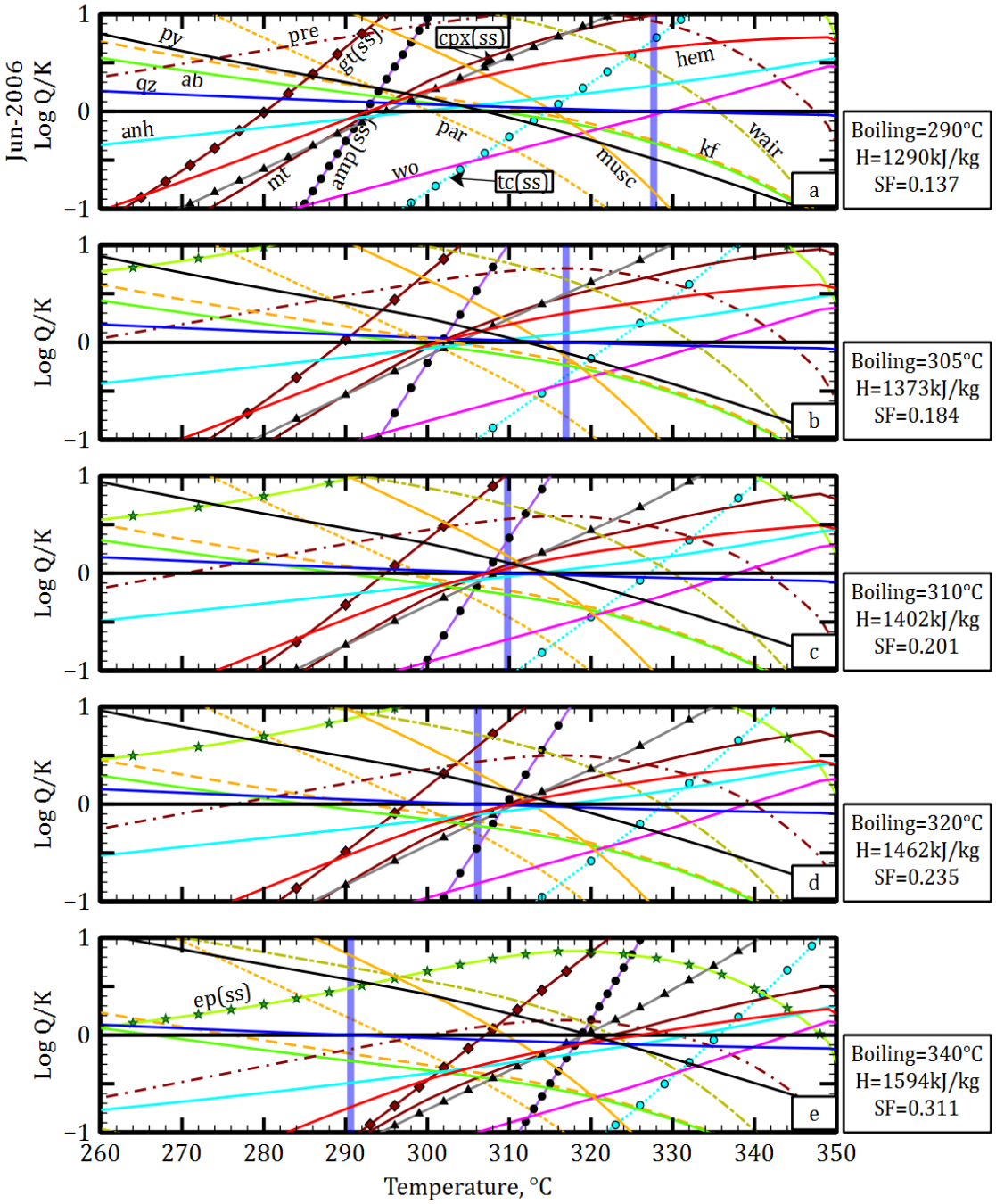

Figure 5. Mineral saturation plots for 2006 sample with varying enthalpy. Each plot the only independent variable to change is the temperature where the onset of boiling occurs, as designated in the lower left of each plot. Mineral abbreviations are shown in Table 3.

The result of increasing the assumed value for total enthalpy to 1595kJ/kg is shown in Graph (e). This enthalpy corresponds to initial boiling at 340°C, and a steam fraction of 0.311, for which the extra added-back steam results in dilution of all dissolved species compared to a steam fraction of 0.137, for the 1290kJ/kg case. This scenario is taken as an extreme for this sample, determined by increasing the enthalpy until quartz saturated at the temperature of boiling within the well (290°C). This shows the large effect that boiling point assumptions have on the estimation of the reservoir temperature. The quartz saturation temperature decreased from 327°C to 290°C, and the mineral cluster discussed above increased from 295°C to 320°C. The decrease in the saturation temperature of quartz is a direct effect of dilution from the extra added-back steam. Most other minerals show the opposite trend, where the addition of extra gases cause the reconstructed fluid to decrease in pH; using an enthalpy of 1290kJ/kg results in a pH of 5.46 at 295°C, but increasing enthalpy to 1594kJ/kg brings the pH down to 5.24 at 295°C.

The tightest convergence for the 2006 reconstruction is achieved by using a wellhead enthalpy of 1402kJ/kg, graph (c), corresponding to a boiling point of 310°C for adiabatic flow. If the fluid did start boiling at 290°C as indicated from P-T logs, this convergence at 310°C suggests a need to investigate the assumption of adiabatic flow within a well. This trend of temperature changes seen in Figure 5 may be a way to estimate an unknown steam fraction to allow for two-phase fluid reconstructions, but that will be left to future studies.

1.2. Wellhead Pure Liquid

Mineral saturation diagrams in graphs (a_1-e_1) of Figure 3 show the equilibrium state for the aqueous phase as sampled at the wellhead as explained in section 4.1 of CHAPTER III. Having analyses of the liquid phase separate from vapor analyses as sampled from the wellhead allows their true compositions at the sampling pressure and temperature to be known. Therefore, our ability to model equilibria within the aqueous phase at the sampling pressure does not depend on assuming that equilibrium between phases was reached. However, applying equilibrium calculations to only the aqueous phase of a two-phase fluid also restricts the meaning of the modeled results to the exact temperature and pressure of sampling, indicated by the red-vertical bar in graphs (a_1-e_1) of Figure 3.

Studies of scale minerals indicate that chalcopyrite, sphalerite, wurtzite and trace galena are precipitating within the pipes at the wellhead(Hardardóttir et al., 2010). If scale precipitation was occurring during each sampling, these minerals must have saturation indices greater than zero at the sampling temperature.

The concentration of copper was not analyzed in the 2004 and 2010 samples, but the 2006 and 2008 samples, graphs (b_1) and (c_1) respectively, show approximate saturation with chalcopyrite. Knowing chalcopyrite is precipitating as scale, its computed saturation in the wellhead liquid validates the computed pH, copper ion and sulfide concentration as analyzed and validates the thermodynamic data involved in its saturation index calculation. However, in these samples, sphalerite and its polymorph wurtzite are highly undersaturated.

This discrepancy may be due to errors in sampling or analyzing zinc concentration, the thermodynamic data for sphalerite and wurtzite, or in thermodynamic data for aqueous zinc complexing. If sphalerite is actually saturated in all samples, the tendency for sphalerite to track consistently with pyrite and chalcopyrite from year to year suggests that the 2012 sample in graph (e_1) is highly supersaturated in chalcopyrite and sphalerite.

Goethite is reported to occur in scale minerals forming downhole in RN-17b and RN-22 (Hardardóttir et al., 2013), and is saturated with the 2008 sample in graph (c_1) of Figure 3, but supersaturated in all others. Exact saturation of the 2008 fluid, with chalcopyrite, and goethite at the sampling temperature may show that the fluid had enough time to reach metastable-equilibrium. Therefore, the amount of deviation from this metastable-equilibrium assemblage in other samples may allow for the determination of the fluid's state of equilibrium at the wellhead. If the 2008 sample reached equilibrium with goethite and chalcopyrite, it would mean that the 2008 fluid as sampled changed the most from the reservoir composition compared to samples from other years where both chalcopyrite and goethite remain supersaturated.

1.3. Maximum Metal Concentrations in Wellhead Reconstructions

The mineral saturation calculations for wellhead fluid shown in Figure 3, indicate that the reservoir fluid is closely represented by the reconstructed fluid. However, the figure also shows that the wellhead fluid has changed from the reservoir conditions because of scale precipitation. Therefore, to use the wellhead

sample to understand copper and zinc concentrations in the reservoir fluid this effect must be accounted for in the reconstruction.

The equilibrium calculations for graphs (a_1-e_1) of Figure 3 show that the thermodynamic data used, SOTHERM, allow the model to treat the precipitation of chalcopyrite accurately, but for sphalerite, the data gives results of undersaturation when in reality it should be saturated. The calculation of sphalerite undersaturation indicates that when calculated at saturation with the thermodynamic data the concentration of zinc will be erroneously high. Therefore, when these minerals are used in this study to calculate the concentration of dissolved copper and zinc, the value for dissolved copper is considered accurate but the value for zinc is considered a maximum.

To account for scale precipitation from the fluid before reaching the wellhead with equilibrium modeling, the scale minerals are assumed to be in equilibrium at depth. For many minerals, this is not appropriate because kinetic precipitation rates may allow oversaturation, but because scale is forming at the wellhead, the maximum concentration of copper and zinc in the downhole fluid must be set by sulfide equilibrium.

CHIM-XPT was used to titrate chalcopyrite, galena, and sphalerite into the reconstructed wellhead fluid until all minerals saturated. Only minerals found as scale were allowed to precipitate, these included the following: chalcopyrite, bornite, pyrite, pyrrhotite, sphalerite, and wurtzite. Of these, chalcopyrite, sphalerite, galena, and pyrite were precipitated after titration, and thus set the values of copper, zinc, lead, and iron for the scale-corrected reconstruction shown in

Table 5. This titration resulted in a copper molality of $9x10^{-7}$, an increase in two orders of magnitude from its previous value of $9x10^{-9}$. A similar increase in zinc is seen, but because pyrite was already at saturation before titration, its concentration decreased slightly accounting for pyrite precipitation. This reconstructed wellhead composition is compared to the downhole sample in the following section.

Table 5. RN-12 wellhead and downhole reconstructed fluid compositions.

Well	RN-12	RN-12[a]	RN-12DH[b]
Date Collected	6/14/2006	6/14/2006	5/9/2007
pH @ 295°C	5.425	5.450	5.967
Aqueous Species (molality)			
H+	4.13E-02	4.13E-02	4.05E-02
H2O	1kg	55.4665	1kg
Cl	5.23E-01	5.19E-01	5.24E-01
SO4	4.73E-04	4.71E-04	5.05E-04
CO2	4.06E-02	4.06E-02	4.06E-02
H2S	1.27E-03	1.27E-03	2.31E-03
SiO2	1.06E-02	1.06E-02	1.00E-02
Al	1.88E-06	1.88E-06	1.01E-04
Ca	3.94E-02	3.94E-02	4.70E-02
Mg	2.68E-05	2.68E-05	3.90E-04
Fe	7.88E-06	4.07E-06	4.30E-04
K	3.45E-02	3.45E-02	3.80E-02
Na	4.06E-01	4.06E-01	3.93E-01
Mn	2.96E-05	2.95E-05	5.20E-05
Zn	2.39E-07	9.50E-06	3.93E-04
Cu	8.59E-09	9.02E-07	2.61E-04
Pb	NA	1.59E-06	1.30E-06
NH4+	9.98E-04	9.97E-04	9.98E-04

[a] Reconstructed wellhead fluid for saturation with chalcopyrite, pyrite, sphalerite, galena at 295°C.

[b] Downhole fluid sample reconstruction. Underlined values based off 2006 wellhead sample. See text for reconstruction method.

2. Understanding Downhole Fluid Samples

Section 1 above, focused on understanding the evolution of the geothermal fluid by analyzing the two-phase fluid sampled at the wellhead. By assuming scale precipitation was the only external effect on the fluid composition during flow to the wellhead, we concluded the section with an approximation for the reservoir-fluid composition after correcting for mineral precipitation. Even with the correction, the wellhead fluid concentrations of dissolved copper and zinc did not reach the values found with the downhole sampler.

For the preceding examination, the wellhead fluid was presumed accurate. In this section, we also assume the downhole sampler to be accurate, and to be representative of the original fluid from which the wellhead fluid samples were derived. Consequently, the decrease in metal concentrations from downhole to wellhead sampling locations must be due to precipitation of minerals. Thus, the discrepancy in metal concentrations can be tested by identifying possible effects of scale precipitation. In the following sections, the downhole sample composition is systematically adjusted for temperature, and pH, to assess the likelihood that those could have contributed to the elevated metal concentrations.

2.1. Downhole Sample Reconstruction

Analytical results from RN-12 downhole sampling, reported by Hardardottir et al. (2009), do not include concentrations of species affected by gas separation: H^+, H_2S, SO_4^{-2}, and CO_2. The concentrations of these species are needed for meaningful thermodynamic calculations, and without them, evaluating the downhole samples for internal consistency under equilibrium constraints is not possible. However, by

knowing what minerals precipitate within the well, and requiring that all composition change between the downhole and wellhead samples is a result of this precipitation, the missing species can be approximated.

Reported sulfide scale minerals found in the Reykjanes system include: chalcopyrite, sphalerite, wurtzite, galena, and pyrrhotite (Hardardóttir et al., 2005, 2013, 2010). The equilibria for these scale minerals are shown in the following equations:

Chalcopyrite:

$$\underset{(cp)}{CuFeS_2} + 0.875\,\underset{(aq)}{H^+} + 0.5\,\underset{(aq)}{H_2O} = \underset{(aq)}{Fe^{++}} + \underset{(aq)}{Cu^+} + 1.875\,\underset{(aq)}{HS^-} - 0.125\,\underset{(aq)}{SO_4{}^{2-}} \qquad (33)$$

$$K = \frac{[a_{Fe^{++}}] * [a_{Cu^+}] * \left[a_{HS^-}^{1.875}\right] * \left[a_{SO_4^{2-}}^{0.125}\right]}{\left[a_{CuFeS_2}\right] * \left[a_{H^+}^{0.875}\right] * \left[a_{H_2O}^{0.5}\right]} \qquad (33a)$$

Sphalerite[a]:

$$\underset{(sl)}{ZnS} + \underset{(aq)}{H^+} = \underset{(aq)}{Zn^{++}} + \underset{(aq)}{HS^-} \qquad (34)$$

$$K = \frac{[a_{Zn^{++}}] * [a_{HS^-}]}{[a_{ZnS}] * [a_{H^+}]} \qquad (34a)$$

Pyrrhotite:

$$\underset{(po)}{FeS} + \underset{(aq)}{H^+} = \underset{(aq)}{Fe^{++}} + \underset{(aq)}{HS^-} \qquad (35)$$

$$K = \frac{[\,a_{Fe^{++}}] * [a_{HS^-}]}{[a_{FeS}] * [a_{H^+}]} \qquad (35a)$$

[a] Wurtzite and sphalerite are polymorphs, so their equilibrium reactions are identical, but their equilibrium constants are different based on their differences in Gibbs free energy.

Galena:

$$\underset{(gn)}{PbS} + \underset{(aq)}{H^+} = \underset{(aq)}{Pb^{++}} + \underset{(aq)}{HS^-} \qquad (36)$$

$$K = \frac{[a_{Pb^{++}}] * [a_{HS^-}]}{[a_{PbS}] * [\, a_{H^+}]} \qquad (36a)$$

These reactions are written so the mineral is related only to species directly specified in the sample analyses given in the APPENDEX and for consistency with the thermodynamic database SOLTHERM. The effect of chalcopyrite precipitation on a fluid composition can be seen in equation (33); for each mole of copper removed from solution by precipitation of chalcopyrite, the following four statements must also be true:

- *0.875 moles of hydrogen ion is added to the solution*
- *0.5 moles of water is added to the solution*
- *1.875 moles of sulfide is removed from solution*
- *0.125 moles of sulfate is removed from solution*
- *1.0 mole of iron is removed from the solution*

Applying the same logic from the above statements to reactions (34) through (35), allows them to be rearranged and solved for the moles of each mineral that must have precipitated between sampling locations to account for the difference in dissolved metals. Rearranging further, the total molar change in copper, lead, and zinc can be used to calculate the total stoichiometric change in each gas species, but to calculate the change in gas species as a result of iron difference requires an additional step.

Iron is tied into both pyrite and chalcopyrite reactions. To find its effect on gas species, total iron must be linked to chalcopyrite through total copper. This is accounted for, by writing an equation for the total change in iron:

$$\Delta Fe_{tot}^{++} = \Delta Fe_{cp}^{++} + \Delta Fe_{po}^{++} \qquad (37)$$

The amount of each mineral to have precipitated between sampling locations is not directly known, but because chalcopyrite is the only copper mineral considered here, its precipitated amount is set by the total change in copper between samples. This allows the effect of pyrrhotite precipitation on hydrogen and sulfide to be written as a function of the total change in, iron, and in copper:

$$\Delta Fe_{po}^{++} = \Delta Fe_{tot}^{++} - \Delta Cu_{cp}^{++} \qquad (38)$$

Combining the stoichiometric relationships of reactions (34) through (35), the concentration of downhole component species, $({}_{\mathrm{DH}}\mathrm{H}^{+}, {}_{\mathrm{DH}}\mathrm{HS}^{-}, {}_{\mathrm{DH}}\mathrm{SO}_4^{2-})$, can be calculated by combining their concentration at the wellhead, $({}_{\mathrm{WH}}\mathrm{H}^{+}, {}_{\mathrm{WH}}\mathrm{HS}^{-}, {}_{\mathrm{WH}}\mathrm{SO}_4^{2-})$, with their change between sampling locations due to the change in dissolved metal concentrations, $(\Delta\mathrm{Pb}^{++}, \Delta\mathrm{Zn}^{++}, \Delta\mathrm{Fe}^{++}, \Delta\mathrm{Cu}^{+})$.

$${}_{DH}H^{+} = {}_{WH}H^{+} + \Delta Pb^{++} + \Delta Zn^{++} + (\Delta Fe^{++} - \Delta Cu^{+}) + 0.875\Delta Cu^{+} \qquad (39)$$

$${}_{DH}HS^{-} = {}_{WH}HS^{-} - \Delta Pb^{++} - \Delta Zn^{++} - (\Delta Fe^{++} - \Delta Cu^{+}) - 1.875\Delta Cu^{+} \qquad (40)$$

$${}_{DH}SO_4^{2-} = {}_{WH}SO_4^{2-} - .125\Delta Cu^{+} \qquad (41)$$

The above equations for downhole concentrations of dissolved hydrogen, sulfide, and sulfate, along with the carbon dioxide concentration from the 2006 wellhead fluid sample, were used to reconstruct the downhole fluid composition,

(Table 5, Table 5. RN-12 wellhead and downhole reconstructed fluid compositions.), thereby allowing its equilibrium condition to be calculated.

In the following three sections, this fluid composition is used as the starting point from which temperature, pH, and sulfide concentration are iteratively changed.

Only sulfide minerals containing Cu, Zn, Fe, and Pb were included in the following equilibrium calculations, to represent the mineral saturation condition when sampled. For a downhole sample analysis to be considered an accurate representation of the fluids at depth, the sample as collected must be a pure aqueous phase. Therefore, any mineral precipitation that occurs in CHIM-XPT calculations at the temperature of sampling will result in a change of fluid composition, and denotes an error in the fluid composition or the modeling results. Allowing only scale minerals in precipitation calculations provides for disequilibrium due to kinetic effects for all other minerals, while requiring scale minerals to obey thermodynamic equilibrium, for which precipitation kinetics are inherently fast to allow precipitation as scale.

2.2. Temperature Effect

Multiphase equilibrium with CHIM-XPT was computed for the downhole reconstruction over a temperature range from 260°C to 400°C. For temperatures below 350°C, the pressure used for calculations was set to the pressure of liquid-vapor saturation. Above 350°C, the pressure was set to 300 bars to prevent boiling; the pressure reset caused offsets in some curves at 350°C on Figure 6.

Modeling results presented in Figure 6 show that the reconstructed

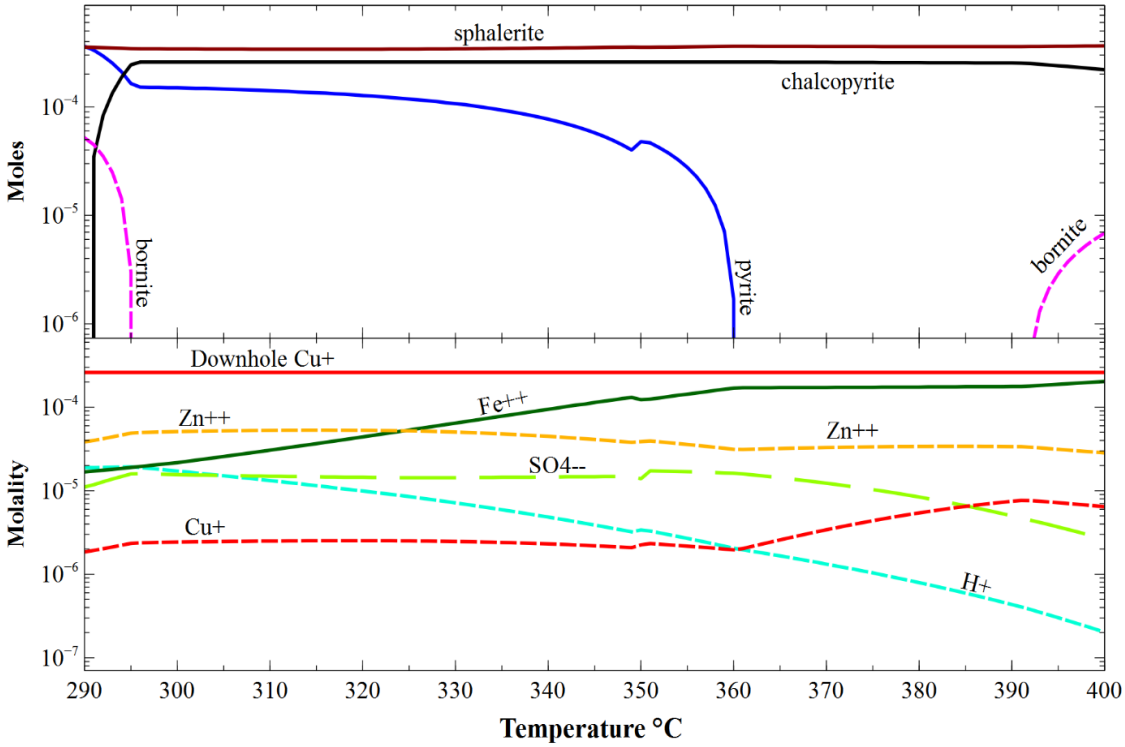

Figure 6. Sulfide mineral equilibrium with the reconstructed downhole fluid for temperatures of 290°C to 400°C. Only minerals observed as scale minerals were included in calculations.

downhole composition is supersaturated with sphalerite and chalcopyrite even when the temperature is raised to 400°C. This relatively small temperature effect on sulfide mineral solubilities suggest that even a large error in the assumed fluid temperature of 295°C, cannot account for the discrepancy between metal concentrations. Therefore, the measured temperature of downhole sampling, 295°C, is used to evaluate pH below.

2.3. pH Effect

The solubility of scale minerals increases with decreasing pH, as evidenced by equilibrium reactions (33) through (35), above. For these reactions, hydrogen

ion and the mineral phase are on the same side, therefore, to satisfy the equilibrium constant, an increase in hydrogen activity must be offset by dissolution of the mineral phase. This pH effect on mineral solubility was explored for the reconstructed downhole fluid by varying the pH from 3 to 6 as shown in Figure 7.

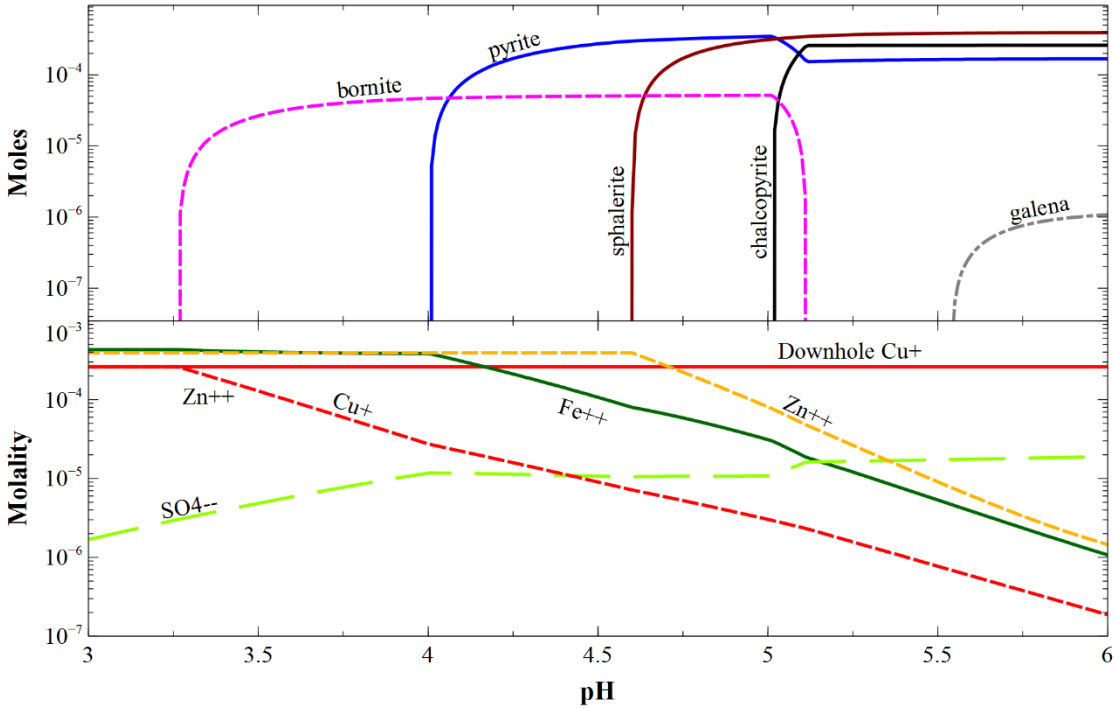

Figure 7. Sulfide mineral equilibrium with the reconstructed downhole fluid for pH ranging from 3 to 6. Calculation of pH change by the addition of HCl to the fluid.

Using CHIM-XPT, pH was iteratively changed while holding temperature constant at 295°C. With each change in pH, the distribution of species was calculated using pH to set the activity of hydrogen ion, which in turn sets total aqueous hydrogen (Reed & Spycher, 1984). By requiring the model to keep a neutral charge, the change in hydrogen ion is offset with an equal change in chloride ion, thus producing acidification of the fluid by addition of hydrogen chloride.

At a pH of 6, galena, chalcopyrite, pyrite, and sphalerite are all calculated to precipitate out of the fluid (Figure 7). At a pH of 5.1 bornite begins replacing chalcopyrite, and continues until a pH of about 5, where chalcopyrite under-saturates. Bornite is fully dissolved when the pH reaches 3.26, at which point the downhole fluid as analyzed is in equilibrium with its dissolved copper concentration. However, a pH of 3.26 is completely unrealistic for fluid from the Reykjanes field as demonstrated below.

If pH buffering during water rock reactions is considered, the expected pH range for the reservoir fluid is between 5.1 and 5.6, when determined using the mineral assemblage found at depth, along with the high concentration of major ions of the fluid.

The minerals that form knots in saturation diagrams of wellhead reconstructions, (Figure 3), match well with minerals found in drill cuttings, (Table 1). Minerals that cross at or close to 295°C for the 2006 wellhead sample consist of quartz, paragonite, anhydrite, microcline, albite, hematite, magnetite, amphibole and pyroxene solid solutions. Of these minerals, a stable mineral pH buffer is formed between quartz, paragonite, and albite.

Quartz and nearly pure albite are reported in the drill cuttings, but paragonite and muscovite are not included in the description of minerals found (Marks, Schiffman, Zierenberg, Franzson, et al., 2010). However, all wellhead samples from RN-12 collected after 2004 include paragonite in the calculated equilibrium mineral assemblage. Therefore it is suspected that the exclusion of paragonite by Marks et al, (2010), is a result of two aggregated issues: the inclusion

of mica in the drilling mud used to prevent circulation loss when the well was drilled making the distinction between contamination difficult (Marks, Schiffman, Zierenberg, Franzson, et al., 2010), and a mechanical sampling bias towards weak minerals, resulting from their pulverization during drilling (Personal Comm, R. Zierenberg 2013)

An equilibrium reaction between albite, paragonite, and quartz is shown in equation (42). The combined reaction between the three minerals only depends on the aqueous ions of sodium and hydrogen.

$$\underset{(ab)}{3\,NaAlSi_3O_8} + \underset{(aq)}{2\,H^+} \leftrightarrow \underset{(par)}{NaAl_3Si_3O_{10}(OH)_2} + \underset{(aq)}{2.0\,Na^+} + \underset{(qz)}{6\,SiO_2} \qquad (42)$$

$$K_{295°C}^{ab\leftrightarrow par} = \frac{[a_{par}] * [a_{Na^+}^2] * [a_{qz}]}{[a_{ab}] * [a_{H^+}^2]} \approx \frac{[a_{Na^+}^2]}{[a_{H^+}^2]} \qquad (43)$$

Therefore, the high sodium concentration in the seawater-derived Reykjanes fluid allows this buffer to resist pH increases until all paragonite in contact with the fluid is used up. Paragonite's saturation in the wellhead fluid samples suggests its presence at depth.

To illustrate the effectiveness of this buffer, log K for the paragonite-albite-quartz buffer was calculated for 295°C and used with the relationship from equation (43) to produce Figure 8. At 295°C, Log K for the paragonite-albite-quartz buffer is 9.28, which sets pH to 5.12 using a sodium activity of 0.107, the activity calculated for the 2006 wellhead reconstruction with SOLVEQ-XPT at 295°C.

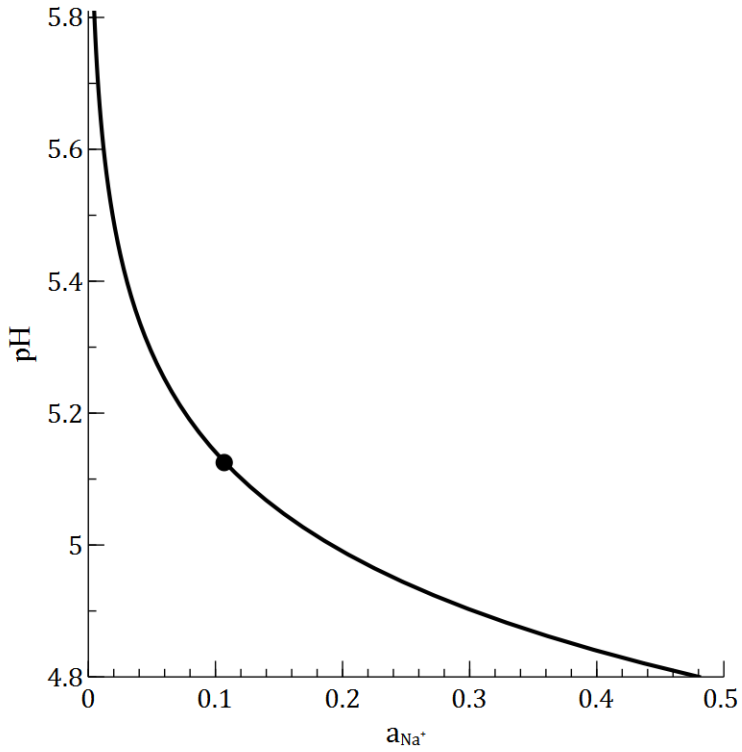

Figure 8. Paragonite–albite–quartz pH buffer calculated for 295°C. Single point of graph for pH of 5.125 assuming sodium activity of 0.106 from the 2006 wellhead sample at 295°C.

The pH of the fluid sampled downhole was probably higher than this, as suggested by the wellhead sample reconstructions. Though close, the minerals are not in exact equilibrium as calculated from the wellhead reconstructions, the state of disequilibrium causing an upward shift in pH from the buffer values. Interestingly, the samples taken in 2008 and later show a much better convergence of solubility curves between the three buffering minerals than the earlier samples do (Figure 3). This pattern is also seen in the calculated pH of the wellhead samples through time plotted in Figure 9, graph (a). From 2004 to 2007, the sample reconstructions had an average pH between 5.5 and 5.6. The samples taken from

2008 through 2012 have a pH values between 5.3 and 5.4, much closer to the pH calculated from the buffering reactions.

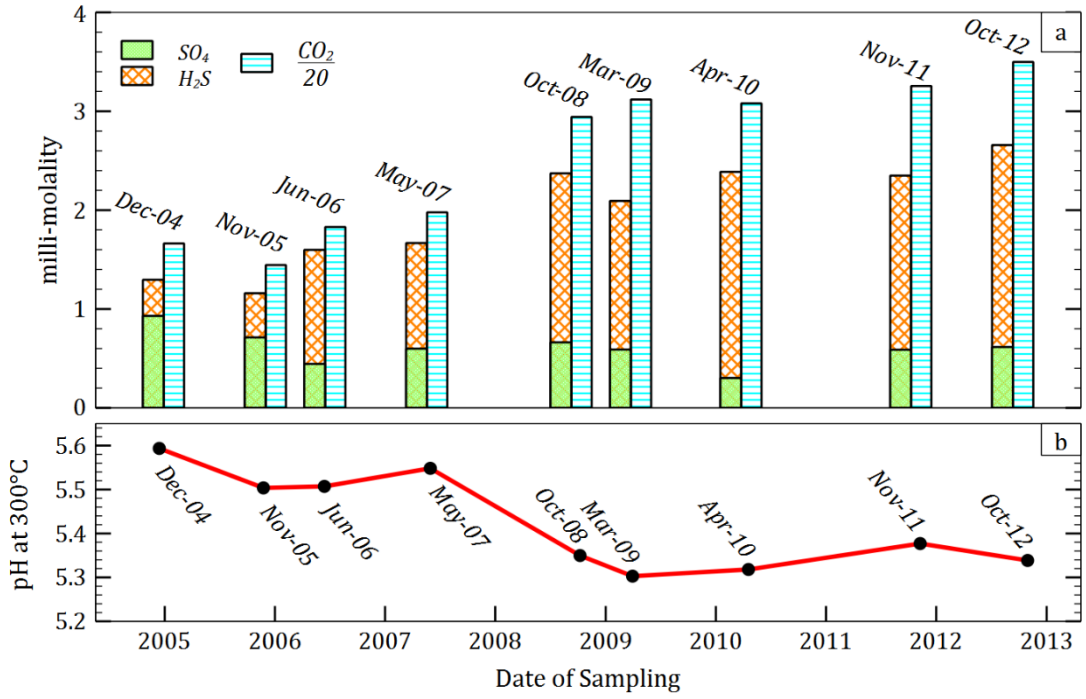

Figure 9. The change in total aqueous SO_4, H_2S, CO_2 (graph a), and pH (graph b), for wellhead fluid reconstructions from samples of RN- 12 taken 2004 to October 2012. Aqueous component species, SO_4, H_2S, and CO_2, (graph a), show an increase in H_2S, and CO_2 and a decrease in SO_4, over time. The modalities for SO_4, and H_2S are plotted to scale, but CO_2 is scale down by 20. Values for SO_4, and H_2S are used in programs SOLVEQ-XPT and CHIM-XPT for accounting of redox reactions and thus their ratio provides insights into changes in oxidation state.

The pH suggested from Figure 7, of 3.26 for the Reykjanes system as understood is not possible, even a pH of 4.6 as needed to bring sphalerite into equilibrium is highly unlikely; instead the likely fluid pH during the downhole sampling was 5.5. This pH corresponds to the values found from the 2004 to 2007 wellhead samples, and also fits perfectly with galena saturation for the reconstructed downhole fluid. The concentration of lead was not addressed above for wellhead reconstructions due to a lack of lead analyses; however, galena

equilibrium as seen here, suggest the total lead measured in the downhole sample could accurately represent the conditions at depth.

In addition to temperature and pH, sulfide-mineral solubilities also depend on the concentration of sulfide in solution, and in turn its oxidation state. If the downhole sampler collected a fluid that contained no sulfate at depth, all sulfide-containing minerals would be undersaturated. In theory, the fluid could mix with another fluid before reaching the wellhead and produce the fluid observed. However, this is improbable for multiple reasons. At the mixing location, the high metal concentrations as measured with the downhole sample would precipitate out causing a point of highly localized scale deposition, for which there is no evidence. In addition, the amount of mixing required would cause the calculated mineral saturation curves for wellhead reconstructions to be smeared out with respect to the temperature of saturation, losing the clustering of minerals seen.

CHAPTER V
CONCLUSIONS

The downhole sample analysis from RN-12 has a dissolved copper molality of 2.61×10^{-4}, a value 289 times greater than the maximum molality of 9.02×10^{-7} calculated for the reservoir fluid as reconstructed from the wellhead fluid in equilibrium with chalcopyrite. The downhole analysis also contains 105 times the iron, and 41 times the zinc than those in the reconstructed fluid.

Using saturation diagrams for wellhead sample analyses of the liquid phase, we show that chalcopyrite scale deposition can be modeled accurately. However, the concentrations we calculate for zinc should be considered a maximum, with actual values even lower. The observation of chalcopyrite and sphalerite scale formation within the wellbore and surface pipes shows that these sulfides form quickly enough to be constrained to equilibrium. Therefore, they cannot be supersaturated at depth, and the maximum concentration of copper and zinc dissolved in the reservoir fluid must be set by equilibria for these minerals.

By using multiple wellhead samples of RN-12, collected from 2004 to 2012, we establish the dynamic nature of the well including: an increasing boiling temperature of 290°C in 2004 to 308°C in 2012 (Figure 3), and a step in pH from 5.5 before 2008, to 5.35 after (Figure 9). However, even with these changing conditions, the wellhead fluid composition can be considered constant between 2004 and 2012 when compared with the downhole fluid composition. This is shown in Figure 10,

where compositions for the reconstructed wellhead and downhole fluids are plotted for multiple dissolved species.

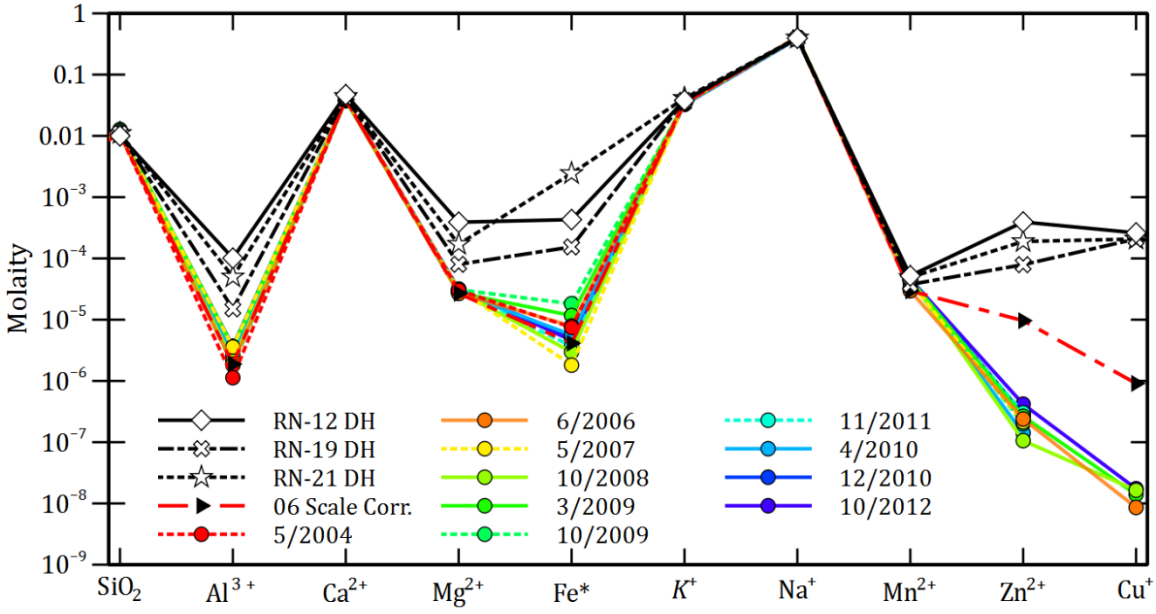

Figure 10. RN-12 Spider diagram of dissolved component species in log scale for reconstructed wellhead analyses from 2004 to 2012, and downhole samples from RN-12, RN-19, and RN-21. All wellhead reconstructions for this plot assume an initial boiling temperature of 295°C and adiabatic flow. The 2006 sample corrected for scale shows the maximum copper and zinc concentrations for equilibrium with chalcopyrite, and sphalerite at 295°C.

For this study, we extend the functionality of equilibrium modeling by computing solid solution compositions, and their saturation indices using only a fluid analysis. With this method, we determine that the wellhead fluid was in contact with, chlorite, garnet, amphibole, and clinopyroxene solid solutions at about 300°C and at compositions that fall in the range determined from RN-17 drill cuttings (Figure 4). The consistency between wellhead sample compositions from 2004 to 2012 and between the fluid composition and drill cuttings suggest the wellhead fluid composition is a reliable representation of the reservoir fluid.

The RN-12 downhole sample analysis does not contain values for dissolved gases, but by combining it with gas data from the 2006 wellhead sample we estimate a complete composition. Using this estimate, the fluid as analyzed is supersaturated with scale minerals up to 400°C, and only by lowering the fluid to a pH of 3.26 does the fluid saturate. However, a pH of 3.26 is not tenable because silicate mineral buffers at depth hold pH between 5.1 and 5.6.

Modeling of the fluid sampled at the wellhead cannot give exact compositions for dissolved metals that are involved with scale deposition because the fluid has changed composition before being sampled. However, by using equilibrium modeling to calculate maximum concentrations, we determine that the concentrations of the copper and zinc in the downhole fluid analysis are not possible for the RN-12 fluid. The consistency of elevated metal concentrations between the three downhole samples shown in Figure 10 suggest a systematic error was introduced from contamination during sampling or analysis.

APPENDIX

WELLHEAD SAMPLE ANALYSES

Table 6. Wellhead sample analyses by Icelandic GeoSurvey, ISOR, from 2004 to 2012. Continued on next page.

Sampling Date	14-Dec-2004	24-Nov-2005	14-Jun-2006	31-May-2007	8-Oct-2008
ISOR Sample #	20040460	20050394	20060387	20070161	20080407
Sampling P	40	40.5	35	30.5	28.5
Liquid Analysis (molality)					
pH, pH temp	5.25, 21.6°C	5.6, 22.3°C	5.72, 22.4°C	5.63, 22.3°C	5.6, 19.1°C
H+	1.79E-03	9.44E-04	8.49E-04	1.16E-03	1.07E-03
H2O	9.98E-01	9.99E-01	9.99E-01	1.00E+00	9.99E-01
Cl	5.543E-01	6.090E-01	6.186E-01	6.327E-01	6.290E-01
SO4	1.93E-04	1.63E-04	1.95E-04	2.01E-04	1.39E-04
CO2	1.84E-03	1.07E-03	9.86E-04	1.45E-03	1.27E-03
H2S	1.57E-04	1.26E-04	1.59E-04	6.19E-05	9.33E-05
SiO2	1.18E-02	1.26E-02	1.25E-02	1.35E-02	1.37E-02
Al	6.67E-07	8.52E-07	2.22E-06	4.34E-06	2.58E-06
Ca	4.27E-02	4.47E-02	4.66E-02	4.77E-02	4.72E-02
Mg	2.88E-05	2.71E-05	3.17E-05	3.78E-05	3.54E-05
Fe	6.84E-06	6.09E-06	9.31E-06	2.18E-06	3.62E-06
K	3.77E-02	3.89E-02	4.08E-02	4.17E-02	4.17E-02
Na	4.411E-01	4.632E-01	4.800E-01	4.933E-01	4.933E-01
Mn	3.64E-05	3.68E-05	3.49E-05	4.93E-05	5.62E-05
Zn	NA	NA	2.83E-07	2.60E-07	1.29E-07
Cu	NA	NA	1.02E-08	NA	2.00E-08
Pb	NA	NA	NA	4.97E-09	NA
NH4+	NA	NA	8.08E-05	NA	8.25E-05
Gas Analysis (mole%)					
H20	9.95E+01	9.95E+01	9.95E+01	9.96E+01	9.95E+01
CH4	6.89E-05	4.26E-05	5.60E-05	1.09E-04	1.15E-04
CO2	4.71E-01	4.21E-01	4.57E-01	3.95E-01	4.78E-01
H2	6.97E-04	5.08E-04	8.95E-04	1.09E-03	5.84E-04
H2S	1.47E-02	1.36E-02	1.66E-02	1.49E-02	1.81E-02
O2	0	8.43E-04	4.71E-05	0	0
NH3	NA	NA	4.92E-04	NA	4.12E-04
N2	1.54E-02	1.48E-02	5.27E-03	6.46E-03	6.45E-03
Ar	2.25E-04	2.21E-04	9.36E-05	1.22E-04	1.21E-04

Table 6. Continued.

Sampling Date	31-Mar-2009	19-Apr-2010	14-Dec-2010	9-Nov-2011	30-Oct-2012
ISOR Sample #	20090059	20100129	20100503	20110405	20120261
Sampling P	31	30.8	30.5	27.5	29.7
Liquid Analysis (molality)					
pH, pH temp	5.48, 21.5°C	5.45, 21.1°C	5.6, 21.6°C	5.82, 22.7°C	5.57, 22.3°C
H+	1.26E-03	1.87E-03	9.49E-04	7.26E-04	1.28E-03
H2O	1.00E+00	1.00E+00	9.99E-01	9.98E-01	9.98E-01
Cl	6.053E-01	6.262E-01	5.889E-01	6.375E-01	6.031E-01
SO4	1.57E-04	1.33E-04	1.46E-04	1.44E-04	1.85E-04
CO2	1.42E-03	2.16E-03	1.11E-03	9.77E-04	1.45E-03
H2S	1.02E-04	7.04E-05	1.03E-04	9.86E-05	1.44E-04
SiO2	1.44E-02	1.36E-02	1.50E-02	1.39E-02	1.38E-02
Al	4.34E-06	3.17E-06	2.62E-06	2.52E-06	4.48E-06
Ca	4.64E-02	4.64E-02	4.67E-02	4.82E-02	4.72E-02
Mg	3.29E-05	3.33E-05	3.62E-05	3.58E-05	3.83E-05
Fe	1.41E-05	6.82E-06	6.43E-06	4.53E-06	5.55E-06
K	4.14E-02	4.02E-02	3.96E-02	4.12E-02	3.96E-02
Na	4.898E-01	4.785E-01	4.728E-01	4.885E-01	4.659E-01
Mn	5.46E-05	5.30E-05	5.55E-05	5.02E-05	5.61E-05
Zn	3.18E-07	1.70E-07	3.46E-07	3.72E-07	5.05E-07
Cu	1.68E-08	NA	NA	NA	2.11E-08
Pb	NA	NA	NA	1.64E-09	NA
NH4+	8.37E-05	7.96E-05	7.79E-05	7.43E-05	7.49E-05
Gas Analysis (mole%)					
H2O	9.95E+01	9.95E+01	9.95E+01	9.95E+01	9.94E+01
CH4	1.24E-04	3.24E-05	1.06E-04	1.32E-04	1.54E-04
CO2	5.15E-01	5.01E-01	4.62E-01	5.07E-01	5.65E-01
H2	5.68E-04	2.71E-04	5.65E-04	7.03E-04	6.21E-04
H2S	1.59E-02	1.86E-02	1.70E-02	1.70E-02	1.97E-02
O2	0	0	0	0	0
NH3	4.04E-04	NA	3.84E-04	3.09E-04	4.70E-04
N2	5.58E-03	2.33E-03	5.14E-03	5.42E-03	5.56E-03
Ar	1.01E-04	6.04E-05	1.04E-04	1.11E-04	1.14E-04

REFERENCES CITED

Anderson, G. M. (2008). *Thermodynamics of natural systems* (2nd ed.). Cambridge University Press.

Driesner, T., & Heinrich, C. A. (2007). The system H2O–NaCl. Part I: Correlation formulae for phase relations in temperature–pressure–composition space from 0 to 1000°C, 0 to 5000bar, and 0 to 1 XNaCl. *Geochimica et Cosmochimica Acta*, *71*(20), 4880–4901. doi:10.1016/j.gca.2006.01.033

Franzson, H., Thordarson, S., Bjornsson, G., Gudlaugsson, S. T., Richter, B., Friðleifsson, G. Ó., & Þórhallsson, S. (2002). Reykjanes high-temperature field, SW-Iceland. Geology and hydrothermal alteration of well RN-10. In *Twenty-Seventh Workshop on Geothermal Reservoir Engineering* (pp. 233–240). Stanford University.

Freedman, A. J. E., Bird, D. K., Arnorsson, S., Fridriksson, T., Elders, W. A., & Friðleifsson, G. Ó. (2010). Hydrothermal minerals record CO2 partial pressures in the Reykjanes geothermal system, Iceland. *American Journal of Science*, *309*(9), 788–833. doi:10.2475/09.2009.02

Fridleifsson, G. O., & Elders, W. A. (2005). The Iceland Deep Drilling Project: a search for deep unconventional geothermal resources. *Geothermics*, *34*(3), 269–285. doi:10.1016/j.geothermics.2004.11.004

Friðleifsson, G. Ó., Elders, W. A., & Albertsson, A. (2013). The concept of the Iceland deep drilling project. *Geothermics*. doi:10.1016/j.geothermics.2013.03.004

Friðleifsson, G. Ó., & Richter, B. (2010). The Geological Significance of Two IDDP-ICDP Spot Cores from the Reykjanes Geothermal Field , Iceland, (April), 25–29.

Friðleifsson, G. Ó., Sigurdsson, Ó., Þorbjörnsson, D., Karlsdóttir, R., Gíslason, Þ., Albertsson, A., & Elders, W. A. (2013). Preparation for drilling well IDDP-2 at Reykjanes. *Geothermics*. doi:10.1016/j.geothermics.2013.05.006

Fridriksson, T., Kristjánsson, B. R., Ármannsson, H., Margrétardóttir, E., Ólafsdóttir, S., & Chiodini, G. (2006). CO2 emissions and heat flow through soil, fumaroles, and steam heated mud pools at the Reykjanes geothermal area, SW Iceland. *Applied Geochemistry*, *21*(9), 1551–1569. doi:10.1016/j.apgeochem.2006.04.006

Fridriksson, T., Oladottir, A., & Jonsson, P. (2010). The Response of the Reykjanes Geothermal System to 100 MWe Power Production: Fluid Chemistry and Surface Activity. *Proceedings World Geothermal Congress*.

Gee, M. A. M., Thirlwall, M. F., Taylor, R. N., Lowry, D., & Murton, B. J. (1998). Crustal Processes: Major Controls on Reykjanes Peninsula Lava Chemistry, SW Iceland. *Journal of Petrology*, *39*(5), 819–839. doi:10.1093/petroj/39.5.819

Hardardóttir, V., Ármannsson, H., & Þórhallsson, S. (2005). Characterization of Sulfide-Rich Scales in Brine at Reykjanes, (April), 24–29.

Hardardóttir, V., Brown, K. L., Fridriksson, T., Hedenquist, J. W., Hannington, M. D., & Þórhallsson, S. (2009). Metals in deep liquid of the Reykjanes geothermal system, southwest Iceland: Implications for the composition of seafloor black smoker fluids. *Geology*, *37*(12), 1103–1106. doi:10.1130/G30229A.1

Hardardóttir, V., Hannington, M. D., & Hedenquist, J. W. (2013). Metal Concentrations and Metal Deposition in Deep Geothermal Wells at the Reykjanes High-temperature Area, Iceland. *Procedia Earth and Planetary Science*, *7*, 338–341. doi:10.1016/j.proeps.2013.03.159

Hardardóttir, V., Hannington, M. D., Hedenquist, J. W., Kjarsgaard, I., & Hoal, K. (2010). Cu-Rich Scales in the Reykjanes Geothermal System, Iceland. *Economic Geology*, *105*(6), 1143–1155.

Holland, T., & Powell, R. (1998). An internally consistent thermodynamic data set for phases of petrological interest. *Journal of Metamorphic Geology*, 309–343.

Johnson, J. W., Oelkers, E. H., & Helgeson, H. C. (1992). SUPCRT92: A software package for calculating the standard molal thermodynamic properties of minerals, gases, aqueous species, and reactions from 1 to 5000 bar and 0 to 1000°C. *Computers & Geosciences*, *18*(7), 899–947.

Marks, N., Schiffman, P., & Zierenberg, R. A. (2011). High-grade contact metamorphism in the Reykjanes geothermal system: Implications for fluid-rock interactions at mid-oceanic ridge spreading centers. *Geochemistry, Geophysics, Geosystems*, *12*(8), n/a–n/a. doi:10.1029/2011GC003569

Marks, N., Schiffman, P., Zierenberg, R. A., Franzson, H., & Friðleifsson, G. Ó. (2010). Hydrothermal alteration in the Reykjanes geothermal system : Insights from Iceland deep drilling program well RN-17. *Journal of Volcanology and Geothermal Research*, *189*, 172–190. doi:10.1016/j.jvolgeores.2009.10.018

Marks, N., Schiffman, P., Zierenberg, R., Elders, W. A., Friðleifsson, G. Ó., & Franzson, H. (2010). Isotopic Evidence of Hydrothermal Exchange and Seawater Ingress from Alteration Minerals in the Reykjanes Geothermal System : Results from the IDDP. *World*, *C*, 15–18.

Palandri, J. L., & Reed, M. H. (2001). Reconstruction of in situ composition of sedimentary formation waters. *Geochimica et Cosmochimica Acta*, *65*(11), 1741–1767.

Pang, Z. H., & Reed, M. H. (1998). Theoretical chemical thermometry on geothermal waters: Problems and methods. *Geochimica et Cosmochimica Acta*, *62*(6), 1083–1091.

Pope, E. C., Bird, D. K., Arnórsson, S., Fridriksson, T., Elders, W. a., & Fridleifsson, G. Ó. (2009). Isotopic constraints on ice age fluids in active geothermal systems: Reykjanes, Iceland. *Geochimica et Cosmochimica Acta*, *73*(15), 4468–4488. doi:10.1016/j.gca.2009.03.033

Rae, A. J., Cooke, D. R., & Brown, K. L. (2011). trace metal chemistry of deep geothermal water, Palinpinon geothermal field, Negros island, Philippines: Implications for precious metal deposition in epithermal gold. *Economic Geology*, (2003), 1425–1446.

Reed, M. H. (1998). Calculation of simultaneous chemical equilibria in aqueous-mineral-gas systems and its application to modeling hydrothermal processes. In J. Richards & P. Larson (Eds.), *Techniques in hydrothermal ore deposits geology* (Vol. 10, pp. 109–124). Reviews in Economic Geology.

Reed, M. H., & Spycher, N. F. (1984). Calculation of pH and mineral equilibria in hydrothermal waters with application to geothermometry and studies of boiling and dilution. *Geochimica et Cosmochimica Acta*, *48*(1982), 1479–1492.

Reed, M. H., Spycher, N. F., & Palandri, J. (2010). SOLVEQ-XPT : A Computer Program for Computing Aqueous-Mineral-Gas Equilibria. *Convergence*, (August).

Rutagarama, U. (2012). *THE ROLE OF WELL TESTING IN GEOTHERMAL RESOURCE ASSESSMENT*.

Shock, E. L., & Helgeson, H. C. (1988). Calculation of the thermodynamic and transport properties of aqueous species at high pressures and temperatures: Correlation algorithms for ionic species and equation of state predictions to 5 kb and 1000°C. *Geochimica et Cosmochimica Acta*, *52*(8), 2009–2036.

Shock, E. L., Sassani, D. C., Willis, M., & Sverjensky, D. A. (1997). Inorganic species in geologic fluids: correlations among standard molal thermodynamic properties of aqueous ions and hydroxide complexes. *Geochimica et Cosmochimica Acta*, *61*(5), 907–50.

Sigurdsson, Ó. (2010). The Reykjanes Seawater Geothermal System–Its exploitation under regulatory constraints. *Geothermal-Energy.org*, (May 2006), 25–29.

Simmons, S. F., & Brown, K. L. (2006). Gold in magmatic hydrothermal solutions and the rapid formation of a giant ore deposit. *Science (New York, N.Y.)*, *314*(5797), 288–91. doi:10.1126/science.1132866

Spycher, N. F., Peiffer, L., Sonnenthal, E. L., Saldi, G., Reed, M. H., & Kennedy, B. M. (2014). Integrated multicomponent solute geothermometry. *Geothermics*, *51*, 113–123. doi:10.1016/j.geothermics.2013.10.012

Wanner, C., Peiffer, L., Sonnenthal, E. L., Spycher, N. F., Iovenitti, J., & Kennedy, B. M. (2013). On the use of Chemical Geothermometry: A Reactive Transport Modeling Study of the Dixie Valley Geothermal Area. *Procedia Earth and Planetary Science*, *7*, 884–887. doi:10.1016/j.proeps.2013.03.107